Assessing submarine groundwater discharge (SGD) and nitrate fluxes in highly heterogeneous coastal karst aquifers: Challenges and solutions

Daniel Montiel, Natasha Dimova, Bartolome Andreo, Jorge Prieto, Jordi Garcia-Orellanac, Valenti Rodellas

Assessing submarine groundwater discharge (SGD) and nitrate fluxes in highly heterogeneous coastal karst aquifers: challenges and solutions

Daniel Montiel[1*], Natasha Dimova[1], Bartolomé Andreo[2], Jorge Prieto[2], Jordi García-Orellana[3, 4], Valentí Rodellas [4, 5]

[1]Department of Geological Sciences, University of Alabama, 35487 Tuscaloosa, USA

[2]Center of Hydrogeology of the University of Malaga (CEHIUMA), 29590 Malaga, Spain

[3]Institut de Ciència i Tecnologia Ambientals (ICTA) Universitat Autònoma de Barcelona, 08193 Bellaterra, Catalunya, Spain

[4]Departament de Física, Universitat Autònoma de Barcelona, 08193 Bellaterra, Catalunya, Spain.

[5]CEREGE, Aix-Marseille Université, CNRS, IRD, Coll France, 13545 Aix-en-Provence, France

Corresponding author: Daniel Montiel

Email address: dmontielmartin@crimson.ua.edu

Tel.: 001 205 861 4772

Postal address: Department of Geological Sciences, University of Alabama, 35487 Tuscaloosa, USA

Email address of coauthors:

Natasha Dimova: ntdimova@ua.edu

Bartolomé Andreo: andreo@uma.es

Jorge Prieto: prieto@uma.es

Jordi García-Orellana: jordi.garcia@uab.cat

Valentí Rodellas: rodellas@cerege.fr

Abstract

Groundwater discharge in coastal karst aquifers worldwide represents a substantial part of the water budget and is a main pathway for nutrient transport to the sea. Groundwater discharge to the sea manifests under different forms, making its assessment very challenging particularly in highly heterogeneous coastal systems karst systems. In this study, we present a methodology approach to identify and quantify four forms of groundwater discharge in a mixed lithology system in southern Spain (Maro-Cerro Gordo) that includes an ecologically protected coastal area comprised of karstic marble. We found that groundwater discharge to the sea occurs via: (1) groundwater-fed creeks, (2) coastal springs, (3) diffuse groundwater seepage through seabed sediments, and (4) submarine springs. We used a multi-method approach combining tracer techniques (salinity, ^{224}Ra, and ^{222}Rn) and direct measurements (seepage meters and flowmeters) to evaluate the discharge. Groundwater discharge via submarine springs was the most difficult to assess due to their depth (up to 15 m) and extensive development of the springs conduits. We

determined that the total groundwater discharge over the 16 km of shoreline of the study area was at least 11 ± 3 × 10^3 m^3 d^{-1} for the four types of discharge assessed. Groundwater-derived nitrate (NO_3^-) fluxes to coastal waters over ~3km (or 20%) in a highly populated and farmed section of Maro-Cerro Gordo was 641 ± 166 mol d^{-1}, or ~75% of the total NO_3^- loading in the study area. We demonstrate in this study that a multi-method approach must be applied to assess all forms of SGD and derived nutrient fluxes to the sea in highly heterogeneous karst aquifer systems.

Keywords: Coastal karst aquifers, submarine groundwater discharge, nitrate fluxes, multi-method approach.

1 Introduction

Coastal karst aquifers are 46% of the Mediterranean coastline, and play a key role in regional socioeconomic, providing residents with essential water resources (Fleury et al., 2007; Bakalowicz, 2015; Arfib and Charlier, 2016; Trezzi et al., 2017). Groundwater is often the only available source as Mediterranean precipitation is scarce and sporadic, and often limited runoff due to efficient infiltration and percolation through the karst aquifers (McCormack et al., 2014).

Typically, karstified carbonate aquifers are comprised of a complex set of fractures, conduits, and cavities generating high spatial and temporal heterogeneity in groundwater flow (Worthington, 1999; Bakalowicz et al., 2005; Barberá and Andreo, 2015). This in turn results in challenging water resources management and attempts to develop water budgets and numerical models describing karst systems often fail or result in estimates with large uncertainties (Butscher and Huggenberger, 2007; Martínez -Santos and Andreu, 2010; Rapaglia et al., 2015).

When a karst system is hydraulically connected to the sea, a significant part of groundwater can flow directly to the sea in different forms (Stringfield and Legrand, 1971; Pinault et al., 2004; Custodio, 2010). Groundwater discharge to the sea can occur via submarine springs (Fleury et al., 2007; Bakalowicz et al., 2008; Dimova et al., 2011) or subaerial coastal springs near the shoreline (Aunay et al., 2003; Mejías et al., 2008; García-Solsona et al., 2010) depending on the geologic structure (Bonacci and Roje-Bonacci, 1997; Benac et al., 2003; Stamatis et al., 2011). Conduits and fractures buried under seabed sediments near the shoreline can also produce diffuse groundwater seepage (e.g. Tovar-Sánchez et al., 2014; Rodellas et al., 2012). Conversely, impervious strata can create enough hydraulic pressure for inland springs whose runoff flows to the sea as groundwater-fed creeks without experiencing infiltration (e.g. Yobbi, 1992; Katz et al., 2009). In this work, we will use the widely accepted term submarine

groundwater discharge (SGD) for the submerged forms of groundwater discharge to the sea as defined by Burnett et al. (2003) and Moore (2010).

Groundwater discharge of unconsolidated sedimentary coastal aquifers has been considered an insignificant component in water and nutrient budgets, mostly due to its relatively small (<10%) volumetric contribution compared to surface water (Burnett and Dulaiova, 2003; Moore 2010). However, in karst systems with limited runoff, SGD is a major component of the coastal aquifer water and nutrient budget. Where excess of nutrients are delivered in coastal systems, these produce ecological perturbations such as harmful algae blooms (e.g. Hallegraeff, 1993; Smith and Swarzenski, 2012), and seagrass habitat modification (e.g.Valiela et al., 1992) to mention a few.

Coastal karst SGD can have very different composition due to the wide range of groundwater residence time and complex pathways of the discharging waters (Weinstein et al., 2011; Tovar-Sánchez et al., 2014; Trezzi et al., 2016). It is therefore necessary to apply a multi-method approach to adequately identify and assess all forms of groundwater discharge when they coexist.

A number of techniques have been developed to identify and estimate groundwater discharge to coastal areas under different climatic conditions and geologic settings. For instance, naturally occurring radon and radium isotopes are effective groundwater tracers of SGD (e.g. Cable et al., 1996; García-Solsona et al., 2010; Rodellas et al., 2015; Dimova et al., 2015) as they are chemically conservative and are typically a few orders of magnitude higher concentrations in groundwater than surface waters, allowing for easy detection in receiving coastal waters (Burnett et al., 2003). Furthermore, mass balance determination of radium and radon excess in near-shore surface quantifies the magnitude of groundwater fluxes (Cable et al., 1996; Wong et al., 2013;

Tovar-Sánchez et al., 2014). Specifically, ^{222}Rn ($t_{1/2}$ = 3.8 d) and ^{224}Ra ($t_{1/2}$ = 3.6 d) which have relatively short half-lives, and in the time-scale range of typical coastal mixing processes can be used in combination to assess SGD (Moore, 1996; Cable et al., 1996; Burnett and Dulaiova, 2003).

Alternatively, in areas of faster groundwater flow regimes (e.g. karst and volcanic systems), salinity (e.g. Knee et al., 2010; Stieglitz et al., 2010; García -Solsona et al., 2010; Dimova et al., 2011) and thermal anomalies along the shoreline at the points of discharge are proven to be good indicators of SGD (e.g. Pluhowski, 1972; Johnson et al., 2008; Peterson et al., 2009; Mejías et al., 2012; Tamborski et al., 2015). In areas where permeable sediments are present, direct measurements of SGD using seepage meters are used in parallel with radiotracer techniques (Lee, 1977; Burnett et al., 2006; Sadat-Noori et al., 2015).

The mixed lithology Maro-Cerro Gordo coastal area is an example where identifying and quantifying all components of groundwater discharge are critical to building a comprehensive water budget that addresses adequately the existing economic and ecological demands of the adjacent coastal communities and ecosystems. Land use includes intensive agriculture with 1.3 km^2 of greenhouses and additional surface tropical crops, in combination with accelerating tourism in the area during the past decades. These land uses are increasingly satisfied by groundwater extractions, in this case from the Sierra Almijara-Alberquillas Aquifer (Andreo and Carrasco, 1993), a highly fissured and karstified marble formation within the study site.

In order to assess the severity and impact of the increasing groundwater abstractions, water managers require a comprehensive water budget for the area. The current water budget based on a mass balance approach indicates total fresh water of 50×10^6 m^3 y^{-1} for the Sierra Almijara-Alberquillas Aquifer (Castillo et al., 2001). This budget was suggested to be comprised

of: (1) inland springs and intermittent creeks (32×10^6 m^3 y^{-1}), (2) extraction for irrigation and consumption purposes (12×10^6 m^3 y^{-1}), (3) water transfer to the Neogene-Quaternary coastal formations, and the remaining part to (4) groundwater discharge to the sea (6×10^6 m^3 y^{-1}). A more recent water mass balance budget using the APLIS (A = altitude, P = slope, L = lithology, I = infiltration landforms, S = soil type) method (Andreo et al., 2008) included an infiltration coefficient of 40 - 45% and confirmed that the total budget of the Sierra Almijara-Alberquillas Aquifer is 50×10^6 m^3 y^{-1} for 2003 – 2005, which were notably dry years (Pérez-Ramos and Andreo, 2007). This assessment based on 2003-2005 data found a slightly higher natural drainage through springs (38×10^6 m^3 y^{-1}) and extraction (15×10^6 m^3 y^{-1}) compared to the estimate by Castillo et al. (2001), suggesting that groundwater discharge is negligible. However, more recently SGD was found to be significant at 1×10^6 m^3 y^{-1} in Maro-Cerro Gordo using a combination of GIS-based approach, hydrometeorological methods, and preliminary ^{224}Ra evaluations (Andreo et al., 2017).

In this study, we performed a comprehensive assessment of the total groundwater discharge to the sea in the Maro-Cerro Gordo area through the application of a set of methods selective to each form of discharge. We used a combination of radiotracers (^{222}Rn and ^{224}Ra) and salinity mass balances, seepage meter measurements, and flowmeter measurements to: (1) identify point discharges to the sea; and (2) quantify the total groundwater dicharge from the Sierra Almijara-Alberquillas Aquifer to adjacent coastal waters. We further (3) estimated groundwater-derived nitrate (NO_3^-) fluxes to the coastal waters of Maro-Cerro Gordo and compared these NO_3^- fluxes in an ecologically protected area (with low anthropogenic activities) to unprotected zones (with intense agriculture and overpopulation). The sampling campaigns were conducted during base flow conditions to provide a conservative estimate of the total

groundwater discharge to the sea and nitrate fluxes of the Sierra Almijara-Alberquillas Aquifer and Maro-Cerro Gordo coastal area. Finally, (4) we compared the applicability of each method to assess the forms of groundwater discharge and made recommendations for applying this approach to other karst aquifer systems worldwide.

2 Study site and hydrogeological settings

The study site, Maro-Cerro Gordo, is located along the coastal fringe between Nerja and La Herradura in the easternmost section of the Malaga Province and part of the western Granada Province (Southern Spain) along 16 km of shoreline (Fig. 1). Approximately 80% of the study area is within the environmentally protected Maro-Cerro Gordo Natural Area, which comprises 3.58 km^2 and 14.31 km^2 of terrestrial and marine surface respectively. The area is characterized by a typical Mediterranean climate with average annual precipitation of 500 mm y^{-1} occurring almost entirely during fall and winter (Andreo and Carrasco, 1993). We have divided the area in three sections based on their predominant lithology and associated forms of discharge. From east to west these are: (1) karst section, which includes the Cerro Gordo cape from Cañuelo Beach to La Herradura; (2) schist section, confined between El Cañuelo Beach and Maro Beach; and (3) conglomerate section, which comprises the area between Maro Beach and Nerja (city) (Fig. 1).

Figure 1: Study site location and geological map showing water table contour lines (from Pérez-Ramos and Andreo, 2007), groundwater flow direction, important wells and piezometers, sampling points, and terrestrial springs. Groundwater discharge to the sea (TGD) is represented in purple and is based on this study. Coastal springs are represented as CS, groundwater-fed creeks as GC, diffuse groundwater seepage as GS, and submarine springs as SS. The study area is divided in

three sections: conglomerate section, schist section, and karst section. The distribution of seagrass beds are based on Bañares-España et al. (2002), and Aranda and Otero (2014).

2.1 Alberquillas Aquifer Unit

The main aquifer formation in the study area is the Alberquillas Aquifer Unit, a telogenetic karst formation that underlines the southeast sector of the Sierra Almijara Aquifer unit and is comprised of highly fissured and karstified Triassic marble (Andreo and Carrasco, 1993). The lithology varies from dolomitic to calcitic marble over the 600 m maximum thickness from basement to the surface (Andreo et al., 1993). In general, the primary porosity of this unit is negligible and the degree of karstification is locally higher in the lower portion, with the exception of Nerja Cave, which is a 3×10^5 m^3 cavity located 158 m above sea level and 930 m from the shoreline (Durán, 1996; Andreo et al., 1993; Jordá et al., 2011).

The Alberquillas Aquifer Unit exhibits an elongated shape towards the southeast and a total surface of 60 km^2, and is directly in contact with the Mediterranean Sea only along the karst section (Fig. 1). The two aquifer units (Alberquillas and Almijara Aquifer units) are hydraulically connected, constituting the Sierra Almijara-Alberquillas Aquifer (142 km^2), which recharges from local precipitation (Carrasco et al., 1998). Conceptual hydrogeological models developed for the Sierra Almijara-Alberquillas Aquifer suggest that groundwater generally flows from north to south, and SGD occurs mainly in eastern Cerro Gordo (Andreo and Carrasco 1993; Carrasco et al., 1998; Pérez-Ramos and Andreo, 2007).

The first attempt to locate SGD in Maro-Cerro Gordo was performed by Espejo et al. (1988) via airborne infrared thermal (IRT) remote sensing. Two thermal anomalies were detected during this survey, one in the Maro area (conglomerate section), and one in the vicinity of Cerro

194 Gordo and Cantarrijan (karst section); these were also confirmed by lower surface seawater
195 salinity (Espejo et al., 1988).

196 A cluster of three submarine caves with active springs (Cantarrijan Caves) were
197 identified at water depths of about 7 m near the Cantarrijan Beach (Fig. 1) during SCUBA diving
198 explorations in the karst section during this study. The vents of these springs are located at the
199 same depth and only 2 – 3 m away from each other. Thus, in our assessments the flux of these
200 three springs was treated as a single discharge point. We identified the vents of two additional
201 submarine springs at water depths of 12 m (Palomas Cave) and 15 m (Sifon Cave) in anchialine
202 caves with up to 10 m of horizontal development (Fig. 1). These caves, together with the three
203 small Cantarrijan Cave springs, represent the deep SGD of Sierra Almijara-Alberquillas Aquifer
204 in the karst section. From SCUBA diving observations, we found that all three discharge points
205 are related to highly-developed karstic conduits at depth. We found during this study that they
206 were active even during droughts (Fig. 2), showing base flow conditions of Sierra Almijara-
207 Alberquillas Aquifer water budget drainage.

208 **2.2 Schist formation**

209 Alberquillas Aquifer Unit is overlaying a concordant Paleozoic schist formation along
210 most of its extension and is tectonically in contact through a set of faults (Andreo et al., 1993).
211 Metamorphosed during the Alpine Orogeny it presents a maximum thickness of 500 m and very
212 low hydraulic conductivity (Andreo et al., 1993). Outcrops of the schist formation can be found
213 almost along the entire schist section (Fig. 1). The schist formation serves as a hydrogeological
214 barrier for SGD in this area (Andreo and Carrasco, 1993), and groundwater discharge to the sea
215 in this section manifests as four small-size creeks and one coastal spring. The four creeks
216 include: Tierras Nuevas Creek which emanates from a soil layer on the schist formation; the

Colmenarejos Creek which was dry over the sampling campaigns; Miel Creek which is of particular interest as it is solely fed by permanently discharging springs located along the Sierra Almijara-Alberquillas Aquifer in the sea (Andreo and Carrasco, 1993). The Maro Stream was observed to be produced by irrigation excess from abundant agriculture located nearby.

Lastly, the Alberquillas coastal spring, located 20 m from the shore at the Alberquillas Beach at the contact between the highly permeable Alberquillas Aquifer Unit karstic marble and impermeable schist, was found to have a perennial flow regime.

2.3 Conglomerate, breccia, and travertine formations

Pliocene conglomerate and breccia deposits with a maximum thickness of 60 m, form ~ 90% of the conglomerate section of the study area, representing the second most important permeable formation in the study site (Fourniguet, 1975; Andreo et al., 1993; Guerra-Merchán and Serrano, 1993). This formation is comprised of marble fragments cemented by a red matrix, showing signs of dissolution in the upper portion due to its calcite composition. Its hydraulic conductivity permits limited groundwater flow mainly due to primary porosity and the slight presence of fractures (Andreo and Carrasco, 1993). In the coastline comprised of this formation, groundwater discharge can be identified visually as two coastal springs, the Doncellas and Barranco Maro Spring and the groundwater-fed creek (Caleta Creek) which originates from a spring located near the town of Maro (Fig. 1). On the easternmost sector of the conglomerate section, south from the town of Maro, a 30 m thick highly porous and permeable quaternary travertine is present in direct contact with the sea at Maro Cliff to the south (Jordá, 1988). The two small coastal springs of Huerto Romero and Maro Beach are present in this formation along with the intermittent groundwater-fed creek of Maro Creek. We have observed that excess water from the Maro Spring located approximately 1 km to the north of Maro Cliff, flows as Maro

Creek and discharges to the sea from the travertine cliff as a waterfall that is intermittently active depending on irrigation times. The Maro Sprig is well-known and it was included in the Sierra Almijara-Alberquillas Aquifer water budget, and it is utilized for drinking and irrigation purposes (Liñán et al., 2000). The Sanguino Creek remained dry throughout this study.

Figure 2: Average monthly precipitation and sea level change during 2010, 215, and 2016. Error bars show the monthly rainfall variability during this study. In December of 2015 slight precipitation occurred only during the first week, however, abundant rainfall took place during September-November. Sea level showed lower values during January-May and higher during August-December. Sampling campaigns were conducted during May-July (dry periods) and December (wet periods).

3 Methods

Water fluxes to the sea from karstic submarine springs were quantified using (1) ^{224}Ra and (2) salinity mass balances, groundwater seepage was quantified using both (3) a ^{222}Rn box model mass balance and (4) seepage meter deployments in the locations where radon anomalies were observed. Subaerial groundwater discharge from coastal springs and groundwater-fed creeks was measured directly using a flowmeter (5).

3.1 Tracer techniques

3.1.1 ^{224}Ra distribution and submarine springs discharge assessment

A total of 38 discreet ^{224}Ra samples of 60 L each were collected in September of 2006 and 2010 to survey the schist and karst sections (Fig. 1). All seawater samples were collected at a depth of 0.3 m, with the exception of SW- 7 and SW-21 that were collected at the submarine springs at 8 m and 15 m respectively. Seawater (n = 30) and groundwater (n = 8) samples were

obtained using a submersible pump, and were later passed through a PVC column filled with about 25 g of MnO_2-coated-fibers (Mn-fibers) at a flow rate of approximately 1 L min^{-1} to allow for a quantitative absorption of ^{224}Ra (Moore, 1976; 2008). Mn-fibers were then transferred to the lab, rinsed with Ra-free water, and partially dried (Sun and Torgersen, 1998). Activities of ^{224}Ra were measured using a Radium Delayed Coincidence Counter (RaDeCC) system (Moore and Arnold, 1996; García-Solsona et al., 2008). The Mn-fibers were counted twice, with the first time immediately after collection to assess the total ^{224}Ra in the water, and a second time after a month to evaluate the supported ^{224}Ra in equilibrium with ^{228}Th. The excess of ^{224}Ra was used to construct a ^{224}Ra mass balance following Charette et al. (2001), which assumes that the ^{224}Ra excess in coastal waters is the result of groundwater inputs (Eq. 1). This approach was applied to assess water fluxes (F_{SGD}, m^3 d^{-1}) originated from the three submarine springs present in the karst section of the study site (Fig 1):

$$F_{SGD} = \frac{\frac{(Ra_{SW} - Ra_{OW}) \times V}{t} + Ra_{SW} \times V \times \lambda}{Ra_{SGD}} \quad (1)$$

where Ra_{sw} is the ^{224}Ra activity in coastal waters, i.e. the surface water end-member (dpm m^{-3}); Ra_{ow} is the offshore ^{224}Ra activity in open waters (dpm m^{-3}); Ra_{SGD} is the activity of the groundwater end-member (dpm m^{-3}); t is the coastal water residence time (d); V is the volume (m^3) of coastal water affected by each submarine spring (SGD plume; and λ is the ^{224}Ra decay constant (0.1894 d^{-1}).

Because this area is greatly exposed to prevailing west winds, large waves, and intensive mixing, we assumed that the residence time (t) of the water in this high energy coastline must be no more than one day. Thus, we used the one-day value in our mass balance model. The volume affected by SGD (V) was constrained using the surface area of the salinity anomaly created by the spring plume and corresponding water depths, obtained from the Andalusia Council of

Environment bathymetry database: http://www.juntadeandalucia.es/medioambiente/site/rediam. To obtain the ^{224}Ra activity (Ra_{sw}) surface water end-member representative of the whole water column, average values of water samples collected from the surface and at the depth of the spring discharge were used.

3.1.2 Salinity anomalies and submarine spring discharge evaluation

To identify and quantify submarine springs discharge following the 1-meter isobath parallel to the shoreline, three salinity boat surveys were performed in May, July, and December of 2015 along the entire stretch of the studied coastline. Electrical conductivity (EC) and temperature (T, ^{o}C) were measured continuously at a constant depth of 0.3 m with accuracies of ± 20 µS cm^{-1} and ± 0.1°C by towing a conductivity-temperature-depth sensor (CTD, Solinst®) from boat at a speed of about 2 km h^{-1}. Seawater salinity values were obtained from EC using the conversion method 2520B (Standard Methods for the Examination of Water and Wastewater, APHA, 1999). Data were recorded in 2 min intervals concurrently with precise GPS boat positioning recorded in 30-sec intervals (Garmin Etrex® 20x) with an accuracy of ± 3 m. Electrical conductivity and temperature of groundwater samples were measured using a Pro2030 (YSI Inc.) handheld instrument with accuracies of ± 1 µS cm^{-1}, and ± 0.3°C. Before sampling, the CTD sensor and handheld instrument (YSI) were calibrated using two conductivity solutions (Oakton®): 1413 µS cm^{-1} and 12,880 µS cm^{-1}, measured at 25˚C. Temperature correction for EC was automatically performed using linear compensations of 2% ˚C^{-1} and 1.91% ˚C^{-1} for the CTD sensor and the handheld instrument respectively.

To compare data points from all surveys and identify consistent spatial salinity variations (i.e. permanent groundwater fluxes) independent of seasonal fluctuations, salinity values from each survey were normalized based on their total average. Salinity anomalies were defined as

positive when salinity is higher than average and negative when it is lower than the average value.

A salinity mass balance based on the salinity anomalies generated by submarine springs inputs was constructed to determine groundwater fluxes (F_{SGD}, $m^3\ d^{-1}$) in the karst section using Eq. 2 and following Crusius et al. (2005) and Knee et al. (2010). To calculate the fresh water fraction of the spring discharge, we used the approach described in Knee et al. (2010), which indirectly defines the groundwater salinity end-member (Sal_{SGD}) to be zero (Eq. 2):

$$F_{SGD} = \frac{\frac{(Sal_{OW} - Sal_{SW}) \times V}{t}}{Sal_{OW}} \quad (2)$$

where, Sal_{ow} and Sal_{sw} represent salinity values of open water and coastal surface waters. As in Eq. 1, V is the volume of coastal water affected by SGD (m^3); and t is the coastal water residence time (d). We used the same end-member values as in the ^{224}Ra mass balance. Note that this mass balance assumes a groundwater salinity end-member (Sal_{SGD}) of zero in order to quantify only the fresh component of SGD (Knee et al., 2010).

3.1.3 ^{222}Rn surveys and groundwater seepage assessment

Seawater ^{222}Rn concentrations were measured in surface coastal waters (at about 0.3 m depth) in July, December of 2015, and July of 2016 along all sections using a RAD AQUA set up (Durridge Co., Inc.) as described in Dulaiova et al. (2005) and further improved by Dimova et al. (2009). To obtain radon-in-water concentrations, the measured radon-in-air was corrected using the temperature-dependent Ostwald's solubility coefficient (Macintyre et al., 1995) (Eq. 3):

$$\alpha = 0.105 + 0.405e^{(-0.05027 \times T)} \quad (3)$$

where T (°C) is the water temperature, measured in 2 min intervals using a temperature data logger (HOBO®, Onset® Inc.). Analytical uncertainties of ^{222}Rn in water were most of the time lower to 10%. The RAD AQUA system was run stationary for at least 20 min at the beginning of

all surveys to achieve water/air and radioactive equilibrium (Dimova et al., 2009), and set up to measure in 10 min intervals while moving at boat speed of 2 km h^{-1} to allow for detection of rapid ^{222}Rn changes. These data were coupled with GPS coordinates to be mapped later.

Diffuse groundwater seepage was quantified using a ^{222}Rn mass balance (box model) as described in Burnett and Dulaiova (2003) during July of 2015 and 2016, and December of 2016. To evaluate diffuse groundwater seepage using a ^{222}Rn mass balance (Eq. 4), ^{222}Rn time-series (1 - 2 days long) were conducted in the Maro Cliff and Cantarrijan Beach seepage area. For this study, this mass balance was modified to account for radon inputs to the sea from a small groundwater-fed waterfall (Maro Creek) (Fig. 1). Radon fluxes (F_{GW}) (dpm m^{-2} h^{-1}) from groundwater discharge were determined using mass balance equation where total ^{222}Rn inputs to the water column are balanced by radon:

$$\mathrm{F_{GW}} = \mathrm{F_{Atm}} + \mathrm{F_{Mix}} - \mathrm{F_{Waterfall}} - \mathrm{C_{Ra}} - \mathrm{F_{Diff}} \quad (4)$$

where F_{Atm} is the ^{222}Rn atmospheric evasion fluxes through the water/air interphase; F_{Mix} are mixing losses due to tidal variations and horizontal mixing; $F_{waterfall}$ are fluxes of ^{222}Rn into the system from a groundwater-fed waterfall present in Maro Cliff; C_{Ra} is the production of ^{222}Rn from ^{226}Ra decay within the water column; and F_{Diff} is ^{222}Rn diffusion flux from seabed sediments.

To assess the contribution of ^{222}Rn from Maro Creek the radon flux from the creek ($F_{waterfall}$) was calculated by multiplying the average creek radon concentration by the water flux which was based of flowmeter measurements and specific area of discharge. This correction was only done during Creek flow regime. Corrections for the production of ^{222}Rn from dissolved ^{226}Ra (i.e. supported radon) in coastal waters (C_{Ra}) were done utilizing the Mn-fiber collected in September of 2006 (one sample) and in July of 2016 (two samples) in Maro Cliff

and Cantarrijan Beach at the time series stations. The average concentration (September 2006 and July 2016) was applied in the ^{222}Rn mass balance. The procedure follows the technique described in details in (Charette et al., 2001). The ^{226}Ra equilibrated samples were counted via gamma spectrometry (HPGe well detector, Canberra GCW3522) using the ^{214}Pb peak at 352 keV. Atmospheric evasion of ^{222}Rn (F_{Atm}) was calculated based on the water/air interphase ^{222}Rn concentration gradient (dpm m^{-3}), ^{222}Rn Ostwald solubility coefficient, and ^{222}Rn gas transfer velocity (k, m h^{-1}). The gas transfer velocity (m h^{-1}) was calculated using Eq. 5 as described in Macintyre et al. (1995):

$$k(600) = 0.45 \times u_{10^{1.6}} \left(\frac{S_c}{600}\right)^{-b} \quad (5)$$

where u_{10} is wind velocity at 10 m above sea level (m s^{-1}) acquired from an internet web service (http://www.wunderground.com/), *Sc* is the Schmidt number, and *b* is a factor that ranges from ½ (u_{10} < 3.6 m s^{-1}) to ⅔ (u_{10} > 3.6 m s^{-1}).

During high wind conditions (July of 2015), we used Eq. 6 (all terms are defined in Eq. 5) designed in Kremer et al. (2003) for shallow waters and a wide range of wind speeds (Cockenpot et al., 2015):

$$k(600) = 1.65 \times e^{(u_{10})} \left(\frac{S_c}{600}\right)^{-b} \quad (6)$$

Molecular diffusion flux of ^{222}Rn from seabed sediments (F_{Diff}) was determined using the approach described in Martens et al. (1980).

After all corrections were made, negative fluxes were considered mixing losses (F_{Mix}). The pore water ^{222}Rn concentration and porosity of sediments were determined based on the procedure reported in Corbett et al. (1998). Groundwater seepage velocity (*SGD*, cm d^{-1}) was then calculated (Eq. 7) by dividing SGD-derived ^{222}Rn fluxes by the representative groundwater ^{222}Rn concentration end-member (Rn_{SGD}, dpm m^{-3}) (Burnett and Dulaiova, 2003).

The groundwater end-member (Rn_{SGD}) was assessed in groundwater collected from a small cavity in the travertine cliff located 1 m a.s.l. in Maro Cliff, and GW-Well in Cantarrijan Beach (Fig.1). Groundwater ^{222}Rn concentrations were analyzed with a RAD7 using a RAD H_2O set up in duplicate 250 mL samples.

$$\mathrm{SGD} = \frac{\mathrm{F_{GW}}}{\mathrm{Rn_{SGD}}} \quad (7)$$

In order to calculate groundwater fluxes (F_{SGD}, $m^3\ d^{-1}$), the obtained seepage velocities were multiplied by the total area through which SGD occurs using Eq. 8:

$$\mathrm{F_{SGD}} = \mathrm{SGD} \times \mathrm{A} \quad (8)$$

where *SGD* represents seepage velocity (cm d^{-1}), and *A* is the seepage area (m^2). To constrain the seepage area (*A*) at the beach face, we conducted a high-resolution ^{222}Rn survey by manually moving a small boat at a speed of 15 m h^{-1}. For more precise results, during this survey, the RAD AQUA system was let to equilibrate for 20 min every 2 - 10 m of shoreline. The high-resolution ^{222}Rn survey data was mapped using a linear ordinary kriging interpolation method (ArcGIS 10), each concentration interval was then contoured (using the ArcGIS 10 contour spatial analyst) to obtain ^{222}Rn concentration isolines. The seepage area (*A*) was delineated by creating a polygon that followed the 35×10^3 dpm m^{-3} isoline as a threshold in Maro Cliff and 6 $\times 10^3$ dpm m^{-3} in Cantarrijan Beach. The seepage area (m^2) was obtained by calculating the polygon geometry based on the ETRS 1989 UTM Zone 30N projected coordinate system.

3.1.4 Fresh SGD assessment in diffuse seepage

As defined by Taniguchi et al. (2002), diffuse groundwater seepage is comprised of two components: (1) a fresh (meteoric) groundwater component and (2) a recirculated seawater component. To calculate the fresh water component in seepage areas of the study site (e.g. in Cantarrijan Beach), we applied a salinity mixing model (Eqs. 9 and 10) as described in

Taniguchi et al., (2005) and used by many others (e.g. Charette et al., 2007; Taniguchi et al., 2008; Santos et al., 2009). The approach relies on two basic equations:

$$f_{FSGD} + f_{RSGD} = 1 \quad (9)$$

$$Sal_{FSGD} \times f_{FSGD} + Sal_{RSGD} \times f_{RSGD} = Sal_{SGD} \times f_{SGD} \quad (10)$$

where f_{FSGD} and f_{RSGD} represent the fresh and recirculated fractions of SGD, and Sal_{FSGD} and Sal_{RSGD} are the salinity values measured in fresh groundwater (GW-Well) and maximum recirculated salinity (GW-Pz-4).

3.2 Direct groundwater flow measurements

3.2.1 Flowmeter measurements of coastal springs and creeks

The location of coastal springs and inland springs feeding groundwater-fed creeks were identified via field observations. The discharge from the identified coastal springs (Doncellas, Barranco Maro, Huerto Romero, Maro Beach, and Alberquillas) and groundwater-fed creeks (Caleta Creek, Tierras Nuevas Creek, and Miel Creek) entering the sea, were measured using a flowmeter (OTT C2, OTT Hydromet GmbH) with an accuracy of ± 10%. Channel widths were between 10 cm and 140 cm and depths were below 30 cm in all springs and creeks. Flow velocity measurements at the average water depths were recorded in 10 cm intervals across the stream cross section right before discharge into the sea. Water fluxes were calculated for each interval multiplying width (10 cm) and depth by flow velocity. Total water flux ($m^3\ d^{-1}$) was then calculated by adding water fluxes in all intervals. To observe differences between dry and wet periods measurements were conducted during July and December of 2016.

3.2.2 Seepage meter measurements of diffuse seepage

To verify ^{222}Rn-based SGD estimates, we deployed multiple seepage meters in July of 2016. Lee-type seepage meters, built following the procedure described in Lee (1977) were

deployed near the ^{222}Rn time series station in areas of active groundwater seepage (Maro Cliff and Cantarrijan Beach) during July of 2016. Four seepage meters were deployed in Maro Cliff and nine in Cantarrijan Beach to obtain a representative evaluation of the seepage area. These were made of a bottomless 60 L plastic drum with an area of 0.12 m^2 with a plastic bag attached to a two-way valve (Isiorho and Meyer, 1999; Schincariol and McNeil, 2002; Rosenberry, 2008). The seepage meters were submerged and slowly inserted in the sediments leaving 2 cm of space between the sediments and the drum interior top. The seepage meter was positioned inclined in order to leave the valve side slightly higher allowing any gas to escape before plastic bag attachment; the water volume entering the plastic bag and time elapsed were then recorded (Lee, 1977). Seepage velocities (*SGD*, cm d^{-1}) were calculated using Eq. 11 modified from Lee (1977):

$$\mathrm{SGD} = \frac{68.79 \times \mathrm{V}}{\mathrm{t}} \quad (11)$$

where *V* is volume of water entering the plastic bag (mL); *t* is the time elapsed (s), and 68.79 is a unit conversion factor specific to the 0.12 m^2 flow area to obtain seepage velocity in cm d^{-1}. Groundwater discharge ($m^3\ d^{-1}$) was calculated using Eq. 8.

3.3 Groundwater chemistry, stable isotopic composition, and NO_3^- fluxes

During July and December of 2015, and in July of 2016 water stable isotopes (δ^2H and $\delta^{18}O$), NO_3^- and SO_4^{2-} were measured in all points of groundwater discharge to the sea, Maro Spring, and a well located in the conglomerate section (Nerja Cave) (Fig. 1). A total of 23 samples were collected in Maro Cliff and Cantarrijan Beach (GW-Well) (n = 4), all subaerial coastal springs (Doncellas, Barranco Maro, Huerto Romero, Maro Beach, and Alberquillas, n = 14), and groundwater-fed creeks (Maro Creek and Miel Creek, n = 5) during all sampling campaigns.

Water samples were collected for analysis in 150 mL bottles and stored at 4°C until measurement, diluted to 1 mS cm^{-1}, and filtered before analysis. NO_3^- and SO_4^{2-} concentrations were analyzed at the CEHIUMA (Center of Hydrogeology of the University of Malaga) laboratory via ionic chromatography (Metrohm 881 Compact IC Pro) with an accuracy of ± 2%. Water stable isotopes (δ^2H and $\delta^{18}O$) were also analyzed at the CEHIUMA using a Laser Cavity Ring-Down Spectrometer (Picarro CRDS L2120-i) with accuracies of ± 1‰ and ± 0.1‰ for δ^2H and $\delta^{18}O$ respectively. Isotopic ratios were calculated using the Vienna Standard Mean Ocean Water (VSMOW, in ‰). Nitrate fluxes ($F_{NO_3^-}$, mmol d^{-1}) to the sea were calculated by multiplying NO_3^- concentrations at each point of discharge during each sampling campaign by corresponding measured groundwater flux (Eq. 12):

$$F_{NO_3^-} = F_{SGD} \times [NO_3^-] \quad (12)$$

where $[NO_3^-]$ represents nitrate concentrations (mmol m^{-3}), and F_{SGD} is the groundwater flux (m^3 d^{-1})

4 Results

4.1 Detecting submarine spring discharge using ^{224}Ra and salinity

4.1.1 ^{224}Ra activities in seawater and groundwater

During the ^{224}Ra sampling campaign in September of 2010, the average ^{224}Ra concentrations in surface waters along the study area was 17 ± 2 dpm m^{-3} (n=30) ranging from 56 ± 4 dpm m^{-3} to 8 ± 1 dpm m^{-3} (Fig. 3; Supplementary material Table A.1). In general, ^{224}Ra values along the schist and karst sections of the study area were lower compared to other Mediterranean regions (e.g. Moore, 2006; García-Solsona et al., 2010; Rodellas et al., 2014). However, two distinctive ^{224}Ra-high anomalies in coastal surface waters were identified during

this survey; these were associated with water inputs with average salinity of 0.8 from the groundwater-fed Miel Creek (56 ± 4 dpm m^{-3}), and the three clustered submarine springs discharging from Cantarrijan Caves (51 ± 4 dpm m^{-3}) located in the Cantarrijan area (Fig. 3). Miel Creek (average salinity anomaly = 0.3), which flows through the marble formation of Alberquillas Aquifer Unit for a total length of approximately 5 km, has a perennial flow, a firm indication that it is fed by groundwater (Fig. 3). Indeed, a set of springs located predominantly in the southernmost section of the Creek at the marble-schist contact have been observed to maintain the constant creek flow regime all year long. The second peak of ^{224}Ra was located right above the three submarine springs (Cantarrijan Caves) near Cantarrijan Beach. Average ^{224}Ra values significantly higher (20 ± 7 dpm m^{-3}) than offshore background activity (8 ± 1 dpm m^{-3}) were detected also along the karst section from Cantarrijan to Cerro Gordo, where Alberquillas Aquifer Unit is directly in contact with the sea (Fig. 3).

Figure 3: Interpolated ^{224}Ra activity concentrations in September of 2010 along the schist and karst sections. Two areas of high ^{224}Ra in coastal waters were identified in the schist section near groundwater-fed Miel Creek (56 ± 4 dpm m^{-3}), and the three clustered submarine springs discharging from Cantarrijan Caves (51 ± 4 dpm m^{-3}) located in the Cantarrijan area (karst section).

Radium-224 in groundwater in Cantarrijan Beach varied from 660 ± 30 dpm m^{-3} (salinity anomaly = 1.6) in a shallow well (GW-Well, Supplementary material Table A.1) to 5500 ± 430 dpm m^{-3} (salinity = 31.1) in five piezometers installed on the shore (GW-Pz-1-5, Supplementary material Table A.1). Activity of ^{224}Ra in groundwater collected from two wells in the karstic marble (GW-CG-1 and GW-CG-2, Supplementary material Table A.1) showed similar activities,

494 1260 ± 90 dpm m^{-3} and 1020 ± 80 dpm m^{-3} with salinities of 2.2 and 0.6 respectively. The
495 variation of ^{224}Ra concentrations in GW-Well and Pz-1-5 (Fig 5c) can be explained by the
496 seawater recirculation in the beach sediments. Radium concentration in fresh waters is very low
497 due to adsorption onto particles. However, in pore water with higher ionic strength (i.e. brackish
498 and salt water) radium desorbs due to cation exchange. This process increases dissolved ^{224}Ra
499 concentration (Webster et al., 1995).

500 **4.1.2 Salinity anomalies**

501 The average salinity in coastal waters of the study site during continuous measurements
502 in September of 2010 was 36.4 ± 0.2, during May of 2015 was 36.6 ± 4.0, in July 2015 was 37.2
503 ± 1.2, and in December of 2015 was 34.5 ± 1.7. A negative salinity anomaly of -1.2 to -1.7 was
504 observed during all sampling campaigns in the conglomerate section in the vicinity of multiple
505 coastal springs (Doncellas, Barranco Maro, Huerto Romero, and Maro Beach) and two
506 groundwater-fed creeks (Caleta Creek, and Tierras Nuevas Creek) (Fig. 4). However, in the
507 schist section where Alberquillas coastal spring enters the sea, salinity was generally similar to
508 the average throughout the coastline with a value of 36.3 in September of 2010, 37.1 in May of
509 2015, 37.1 in July of 2015, and 34.4 in December of 2015. Similarly, small salinity variation
510 (Fig. 4) associated with high ^{224}Ra (Fig. 3) was observed near the outlet of the groundwater-fed
511 Miel Creek.

512

513 **Figure 4: Salinity anomaly map showing combined results from May, July, and December of 2015.**
514 **Two areas of negative salinity anomalies were found in the conglomerate (salinity anomaly = -1.2 to**
515 **-1.7) and karst (salinity anomaly = -0.3 to -1.0) sections almost perfectly aligned with their**
516 **delineated extent.**

517

In the karst section (Fig. 1), where the karstic marble formation is in contact with the sea, negative salinity anomalies (-0.3 to -1.0) coincided with previously observed high ^{224}Ra concentrations in coastal waters near the Palomas and Sifon Caves submarine springs. The largest salinity anomaly (-1.0) in the karst section was found in Cantarrijan Beach, which could be related to Cantarrijan Caves springs. However, the lowest values are distributed along the beach area, slightly deviated to the East off Cantarrijan Caves, where groundwater seepage through marine sediments can, therefore, also be occurring.

4.2 Evaluating submarine spring discharge using ^{224}Ra and salinity

4.2.1 ^{224}Ra mass balance

To assess groundwater discharge in the areas of high ^{224}Ra (12 – 51 dpm m^{-3}) and negative salinity anomalies (-0.3 to -1.0), i.e. the areas of Cantarrijan Caves, Palomas Cave, and Sifon Cave submarine springs (Figs. 2 and 3), we used a ^{224}Ra mass balance following Moore (1996) and Charette et al. (2001; Eq.1). The main assumption in this approach is that the ^{224}Ra excess in the karst section is considered to be originated solely by submarine springs.

SGD through Cantarrijan Caves was quantified using the ^{224}Ra coastal water end-member measured in SW-6, SW-7, SW-13 and SW-24 (Ra_{sw} = 25 ± 2 dpm m^{-3}, n = 4), where SW-7 was collected at the depth of discharge (8 m). Average offshore background activity (8 ± 1 dpm m^{-3}) measured in SW-23, SW-27, SW-29, and SW-30 was used as the open water end-member (Ra_{ow}) (Supplementary material Table A.1). Groundwater samples collected from well GW-CG-1 (Fig.1), which is the closest well to the submarine springs and is representative of the marble aquifer formation, was used as the groundwater end-member (1260 ± 90 dpm m^{-3}, salinity = 2.2). Following the same approach, SGD was also evaluated in the area of Palomas Cave using SW-SW-20, SW-21, and SW-25 (Ra_{sw} = 18 ± 2 dpm m^{-3}, n = 3), where SW-21 was collected at 15 m

depth of discharge. In Sifon Cave samples SW-14, SW-22, and SW-26 were used as the coastal water end-member. The same open water (Ra_{ow}) and groundwater (Ra_{SGD}) end-members were used: 1260 ± 90 dpm m^{-3} and 8 ± 1 dpm m^{-3} respectively (Fig. 3; Table 1).

The estimated groundwater fluxes (F_{SGD}) through Cantarrijan Caves was 4.7 ± 0.5 × 10^3 m^3 d^{-1}, at Palomas cave was 4.3 ± 0.5 × 10^3 m^3 d^{-1}, and for Sifon Cave was 3.7 ± 0.4 × 10^3 m^3 d^{-1}. This represents a total flux of 12.8 ± 1.4 × 10^3 m^3 d^{-1} via submarine springs, where reported errors are based on analytical uncertainties of ^{224}Ra measurements.

4.2.2 Salinity mass balance

The salinity anomaly created by the Cantarrijan, Palomas, and Sifon Caves in the karst section (Fig. 4, Table 1) allowed us to construct individual mas-balances at each location and calculate SGD independently of the ^{224}Ra approach. Considering that the salinity of groundwater discharge of these springs is the same value of the endmember used for the ^{224}Ra method (Table 1), and applying Eq. 2 we calculated a total groundwater flux of 0.8 ± 0.1 × 10^3 m^3 d^{-1} in Cantarrijan Caves, 0.9 ± 0.1 × 10^3 m^3 d^{-1} in Palomas Cave, and 0.5 ± 0.1 × 10^3 m^3 d^{-1} through Sifon Cave; representing a total of 2.3 ± 0.2 × 10^3 m^3 d^{-1}.

4.3 Assessing diffuse groundwater seepage using a ^{222}Rn mass balance and seepage meter measurements

4.3.1 ^{222}Rn distribution in seawater

High ^{222}Rn concentrations were measured in two distinct areas in the Maro Cliff area (conglomerate section) and Cantarrijan Beach (karst section) with maximum concentrations of 44 ± 3 × 10^3 dpm m^{-3} and 30 ± 2 × 10^3 dpm m^{-3} respectively (Fig. 5). In general, along the conglomerate section, ^{222}Rn activities were within background levels (1.9 ± 0.6 × 10^3 dpm m^{-3}) with the mentioned exception of a cove in the Maro Cliff area where the travertine formation is

in contact with the sea. In this location, a 15-m travertine cliff ends in coarse seabed sand through which groundwater seepage was identified underlying a 1.5-m water column. In the karst section, high ^{222}Rn was detected only along the Cantarrijan Beach where a steep ravine, formed in the marble formation, ends in a big opening comprised of coarse sand, pebbles, cobbles, and even boulders suggesting flash flooding events in the ravine after significant precipitations.

Figure 5: Radon-222 distribution map based on surveys during July and December of 2015, and July of 2016. Two radon peaks were in found in Maro Cliff (conglomerate section) and Cantarrijan Beach (karst section) with maximum concentrations of 44 ± 3 × 10^3 dpm m^{-3} and 30 ± 2 × 10^3 dpm m^{-3} respectively.

4.3.2 Groundwater discharge assessments in the conglomerate section (Maro Cliff)

Diffuse groundwater seepage was identified in this area during all ^{222}Rn surveys (July and December of 2015, and July of 2016) suggesting the seepage is maintained by base groundwater flow (Fig. 6a). We calculated that ^{222}Rn contribution from the waterfall (i.e., $F_{Waterfall}$) was on average 16 ± 6 dpm m^{-2} d^{-1}(Table 2). To account for the production of ^{222}Rn from ^{226}Ra dissolved in coastal waters (C_{Ra}), we used the averaged concentration (280 ± 50 dpm m^{-3}, n = 3) measured in September of 2006 (306 ± 40 dpm m^{-3}, n = 1) and July of 2016 (260 ± 50 dpm m^{-3}, n = 2) at the time series station (Table 2, Fig. 6b). Atmospheric evasion (F_{Atm}) was calculated using Eq 8 except in July of 2015, when wind speed was much higher (8 m s^{-1}) and we used Eq. 6 instead. Diffusive flux of ^{222}Rn from seabed sediments (F_{Diff}) was 619 ± 57 dpm m^{-2} d^{-1} accounting for only 0.2 – 0.5% of total ^{222}Rn fluxes (Fig. 7). As one would expect in coastal

588 waters with little protection against wind and waves, mixing losses in this study represent the
589 main ^{222}Rn loss in the model (Fig. 7).
590
591 **Figure 6: (a) Groundwater seepage velocity averaging results from radon mass balance and seepage**
592 **meters in areas of diffuse seepage (Maro Cliff and Cantarrijan Beach). Radon distribution in (b)**
593 **Maro Cliff (conglomerate section) and (c) Cantarrijan Beach (karst section) where cylinder**
594 **symbols represent seepage meter locations and the star radon time series stations.**
595
596 The ^{222}Rn concentrations in groundwater end-members (Rn_{SGD}) were 350 ± 50 × 10^3 dpm
597 m^{-3}, 440 ± 60 ×10^3 dpm m^{-3}, and 320 ± 30 × 10^3 dpm m^{-3} during July, December of 2015, and
598 July of 2016 respectively, with an average value of 370 ± 50 × 10^3 dpm m^{-3}. Based on these
599 estimates (Table 2) and applying Eq. 4, we obtained average seepage velocities of 39 ± 10 cm d^{-1}
600 (n = 43) in July 2015, 40 ± 11 cm d^{-1} (n = 78) in December of 2015, and 38 ± 10 cm d^{-1} (n = 90)
601 during July of 2016. Reported SGD uncertainties are calculated based on ^{222}Rn variations from
602 all samples collected in the area to obtain the groundwater end-members (Rn_{SGD}) (Burnett et al.,
603 2007); which ranged from 320 ± 30 × 10^3 dpm m^{-3} to 690 ± 50 × 10^3 dpm m^{-3} (n = 8) during this
604 study.
605 Utilizing Eq. 8 we estimated total groundwater fluxes based on the ^{222}Rn box model to be
606 3.0 ± 0.8 × 10^3 m^3 d^{-1} during July of 2015, 3.1 ± 0.8 × 10^3 m^3 d^{-1} in December of 2015, and 2.9 ±
607 0.7 × 10^3 m^3 d^{-1} in July of 2016 (Table 2). Using Eq. 11 an average seepage velocity of 28 ± 6 cm
608 d^{-1} (Table 3) was calculated. This assessment is in good agreement with the average ^{222}Rn-based
609 value of 38 ± 10 cm d^{-1}. Using Eq. 8 and a seepage area of 7.7 × 10^3 m^2 based on the radon
610 concentration (Fig. 6b), we calculated a groundwater flux of 2.1 ± 0.4 × 10^3 m^3 d^{-1} in July of
611 2016 (Table 3).

4.3.3 Groundwater fluxes in the karst section (Cantarrijan Beach)

Multiple radon surveys in this area (July and December of 2015, and July of 2016) indicated a strong seasonality in seawater ^{222}Rn concentrations, with an average of 75 ± 3 × 10^3 dpm m^{-3} in December and 11 ± 2 × 10^3 dpm m^{-3} in July, suggesting higher SGD during the wet period. The average ^{226}Ra concentration (C_{Ra}) was 170 ± 40 dpm m^{-3} measured in September of 2006 (169 ± 30 dpm m^{-3}, n = 1) and July of 2016 (170 ± 40 dpm m^{-3}, n = 2) (Table 2). The variation of the groundwater ^{222}Rn end-member (240 ± 60 × 10^3 dpm m^{-3} to 350 ± 40 × 10^3 dpm m^{-3}, n = 6) was used to calculate the final groundwater discharge flux uncertainties. Seepage velocities in December and July were on average 52 ± 8 cm d^{-1} (n = 61) and 22 ± 3 cm d^{-1} (n = 115) respectively (Table 3).

We found that groundwater seepage occurs only in the westernmost sector at the end of the Cantarrijan Ravine (Fig. 6c). Seepage velocities, determined from all seepage meters deployed along the beach, show that groundwater seepage ceases exactly at the location where seepage meter SM-4 was deployed (Fig. 6c). We used this as a criterion to define the seepage face and decided to use the ^{222}Rn contour line of 6 ± 1 × 10^3 dpm m^{-3} to calculate the seepage area, and averaged SM-1-4 to determine a seepage velocity of 23 ± 7 cm d^{-1}. Using the ^{222}Rn method we found that the total diffuse groundwater seepage in the Cantarrijan Beach area ranged from 2.3 ± 0.3 × 10^3 m^3 d^{-1} during the wet period to 0.9 ± 0.1 × 10^3 m^3 d^{-1} during dry conditions; whereas seepage meter measurements resulted in 0.9 ± 0.2 × 10^3 m^3 d^{-1}.

Figure 7: Radon fluxes result of each component of the mass balance box model during all sampling campaigns in Maro Cliff (conglomerate section) and Cantarrijan Beach (karst section). The largest tracer losses occurred via mixing due to the high exposure of both areas to waves and currents.

Greater difference in SGD-^{222}Rn fluxes was found between wet periods (December) and dry periods (July) in Cantarrijan Beach compared to Maro Cliff.

During all sampling campaigns, the groundwater sampled from the shallow well at Cantarrijan Beach (GW-Well, Fig.1) always had salinity values of 1.6 – 3.2. During September of 2010, salinities of 6.6 – 31.1 were also observed in pore water samples collected in all five piezometers installed on the beach (GW-PZ-1-5, Fig 1). Based on the salinity mixing model (using Eqs. 9 and 10) we calculated that the fresh fraction of SGD at this site was 48% of the total groundwater seepage. Therefore, when constructing the Sierra Almijara-Alberquillas Aquifer freshwater water budget for July of 2016, only 0.4 ± 0.1 × 10^3 m^3 d^{-1} (representative of the 48% freshwater component) should be taken into account.

4.4 Groundwater contribution from coastal springs and groundwater-fed creeks

Groundwater discharge to the sea during dry conditions calculated using flowmeter measurements in July of 2016 from coastal spring Huerto Romero was 37 ± 3 m^3 d^{-1}, from Maro Beach was 26 ± 2 m^3 d^{-1}, from Barranco Maro was 17 ± 1 m^3 d^{-1}, from Doncellas was 460 ± 40 m^3 d^{-1}, and from Alberquillas was 1060 ± 90 m^3 d^{-1} (Supplementary material Table A.2). The discharge from groundwater-fed creek Miel Creek was 1230 ± 110 m^3 d^{-1}, from Caleta Creek 160 ± 10 m^3 d^{-1}, and from Tierras Nuevas Creek was 110 ± 10 m^3 d^{-1}. The total discharge from all creeks was 3100 ± 280 m^3 d^{-1}; which represents 33% of the total groundwater discharge in the study area.

In December of 2016, during high flow conditions, discharge from coastal springs Huerto Romero was 100 ± 9 m^3 d^{-1}, from Maro Beach was 43 ± 4 m^3 d^{-1}, from Barranco Maro was 69 ± 6 m^3 d^{-1}, from Doncellas was 530 ± 50 m^3 d^{-1}, and from Alberquillas was 1590 ± 140 m^3 d^{-1}. Discharge via groundwater-fed Miel Creek was 1820 ± 160 m^3 d^{-1}, from Caleta Creek was 220 ±

659 20 $m^3 d^{-1}$, and from Tierras Nuevas Creek was 190 ± 20 $m^3 d^{-1}$; which constitutes 4580 ± 60 m^3
660 d^{-1} or 37% of the total discharge in the study area (Supplementary material Table A.2).
661
662 **4.5 Groundwater isotopic composition, water chemistry, and nitrate fluxes**Isotopic
663 values are widely scattered along a linear trend (Local Groundwater Line, LGL) with a slope of
664 6.06, with averages of -42‰ and -7.1‰ for δ^2H and $\delta^{18}O$ respectively (Figs. 8a and 8b). All
665 samples fall between the Global Meteoric Water Line (GMWL; Craig, 1961) and the Western
666 Mediterranean Meteoric Water Line (WMMWL; Gat and Garmi, 1970), samples collected in or
667 derived from Maro Spring are situated slightly above the WMMWL. Deuterium values ranged
668 from -33 ± 1‰ to -46 ± 1‰, while $\delta^{18}O$ were between -5.6 ± 0.1‰ and -7.8 ± 0.1‰
669 (Supplementary material Table A.2). We observed that groundwater collected from Maro Spring
670 (conglomerate section) has the lightest isotopic signature of. -46‰ and -7.7‰ for δ^2H and $\delta^{18}O$
671 respectively. Samples collected in the conglomerate section from coastal springs Barranco Maro,
672 Huerto Romero, Maro Beach, and groundwater-fed Maro Creek showed values that ranged from
673 -45 and -7.6 to -43‰ and -7.2‰. At the point of seepage discharge in the sea, Maro Cliff showed
674 slightly higher values of -44‰ and -7.4‰ for δ^2H and $\delta^{18}O$. Coastal springs Doncellas,
675 Alberquillas, and groundwater-fed Miel Creek all located in the schist section, are grouped
676 together with Nerja Cave (conglomerate section), showing average values of -33‰ and -5.5‰
677 for δ^2H and $\delta^{18}O$. Samples collected from GW-Well (Cantarrijan Beach), have the highest values
678 in the study area with averages of -22‰ and -3.8‰ for δ^2H and $\delta^{18}O$.
679
680 **Figure 8: (a) Isotopic composition ($\delta^{18}O$, δ^2H) of water samples collected during all sampling**
681 **campaigns. Local Groundwater Line (LGL) represents the linear trend based on all groundwater**
682 **samples collected in the study area. Global Meteoric Water Line (GMWL) is based on Craig, (1961)**

and the Western Mediterranean Meteoric Water Line (WMMWL) on Gat and Garmi, (1970). White color represents points of discharge in conglomerate and breccia lithology, while light grey are in travertine (conglomerate section); dark grey shows points in schist (schist section); and black color show locations in karstic marble (karst section). Maro Spring and Nerja Cave well (not points of discharge to the sea) are represented with a black and white star respectively. Water samples collected at each section (conglomerate section, schist section, ans karst section) are grouped in dashed squares. (b) Isotopic composition of samples collected from points of discharge from the travertine formation in the conglomerate section. The two groundwater end-members (Maro Spring and irrigation waters) are circled, while diffuse seepage in Maro Cliff is represented with squares.

Groundwater sulphate (SO_4^{2-}) concentrations ranged from 500 ± 10 mmol m^{-3} in Alberquillas coastal spring to 3220 ± 64 mmol m^{-3} in Cantarrijan Beach (n = 23) (Supplementary material Table A.2). Samples collected in the conglomerate section from coastal springs Doncellas, Barranco Maro, Huerto Romero, Maro Beach; groundwater-fed Maro Creek, and diffuse seepage in Maro Cliff had similar SO_4^{2-} concentrations ranging between 1500 and 3000 mmol m^{-3}. All samples (including Maro Spring) collected from Sierra Almijara-Alberquillas Aquifer in this area fall within a SO_4^{2-} concentration range of 1700 – 2600 mmol m^{-3}. Miel Creek and coastal spring Alberquillas (schist section) showed lower values ranging from 500 ± 10 to 710 ± 14 mmol m^{-3}. Water collected in Cantarrijan Beach had the highest concentration in the study area, with an average of 3030 ± 60 mmol m^{-3} (Supplementary material Table A.2).

Nitrate (NO_3^-) concentrations were highest in coastal springs of the conglomerate section including Doncellas, Barranco Maro, Huerto Romero, and Maro Beach with an average of 446 ±

50 mmol m^{-3} (n = 6). Water samples that were directly derived from Maro Spring (Maro spring, Maro Creek) and did not experience infiltration (i.e. had no fertilizer added), showed NO_3^- concentration of 5 – 21 mmol m^{-3}.NO_3^- concentrations in diffuse groundwater seepage in Maro Cliff were consistently near 130 ± 3 mmol m^{-3} (n = 2). Samples collected in the schist section from groundwater-fed Miel Creek and coastal spring Alberquillas, and in the karst section from Cantarrijan Beach, showed levels of NO_3^- ranging from 55 mmol m^{-3} in Miel Creek to 168 mmol m^{-3} in Cantarrijan Beach (n = 5) (Supplementary material Table A.2).

Nitrate fluxes were unevenly distributed in the three sections of the study site (Table 4). The combination of high NO_3^- in coastal springs and high flow groundwater seepage results in NO_3^- fluxes in the conglomerate section of 550 ± 140 mol d^{-1} and 730 ± 190 mol d^{-1}. During this study, NO_3^- fluxes in the schist and karst section together were 150 ± 20 mol d^{-1} during dry and 250 ± 40 mol d^{-1} during wet periods (Table 4).

5 Discussion

5.1 Method selection and assessment of each form of groundwater discharge to the sea

Submarine springs: Quantifying submarine springs discharge in the karst section was found to be the most difficult part of this study. None of the data collected during the three ^{222}Rn boat surveys along the coastline showed tracer anomalies in the areas of submarine spring discharge (Fig. 5). However, we were able to detect ^{224}Ra and salinity anomalies produced by the three submarine springs discharging from Cantarrijan, Palomas, and Sifon Caves (Fig. 3 and 4). Concentrations of ^{224}Ra were on average four times higher (20 ± 7 dpm m^{-3}, n = 10) compared to offshore waters (8 ± 1 dpm m^{-3}, n = 4) in locations where no ^{222}Rn signal was detected.

730 Considering that ^{224}Ra and ^{222}Rn have similar half-lives and experience similar mixing,
731 we hypothesize that the lower ^{222}Rn concentrations in coastal waters of the karst section must be
732 due to degassing. Similar effects on dissolved ^{222}Rn and ^{224}Ra have been observed in coastal
733 waters by Dulaiova and Burnett (2006) and Stieglitz et al. (2010). As found in this study site,
734 both studies showed a strong correlation between ^{222}Rn concentration and salinity or ^{222}Rn
735 and ^{224}Ra, trends that are consistent with a ^{222}Rn deficiency due to atmospheric evasion (Stieglitz
736 et al, 2010). Furthermore, when combining the ^{222}Rn concentration data with salinity anomalies
737 from all boat surveys along the entire shoreline, we observe that ^{222}Rn concentrations decrease at
738 a faster rate than salinity when closer to the groundwater source (Fig. 9a, b). If wind conditions
739 are constant during the surveys (which there were), following the 1st Fick's Law, degassing due
740 to molecular diffusion through the water-atmosphere interphase must be enhanced when
741 seawater ^{222}Rn concentration is higher (the concentration gradient is higher). Thus, this effect is
742 most likely created because the water column-atmosphere concentration gradient in areas close
743 to the groundwater source is at its highest, favoring atmospheric evasion.
744
745 **Figure 9: Mixing plots of ^{224}Ra (a) and ^{222}Rn versus salinity (b) showing best fit linear and**
746 **exponential mixing lines, respectively, during surface water surveys along the coastline in**
747 **September of 2010, July and December of 2015.**
748
749 Based on these findings, we concluded that ^{224}Ra (Eq. 1) and salinity (Eq. 2) mass
750 balances are the two methods better suited to evaluate groundwater discharge from submarine
751 springs of the ones utilized in this study. However, we found a significant difference between the
752 springs discharge assessments obtained using these two tracers; the flux based on the ^{224}Ra mass
753 balance was $12.8 \pm 1.4 \times 10^3$ m^3 d^{-1}, whereas using the salinity mass balance we calculated a

discharge of 2.3 ± 0.2 × 10^3 m^3 d^{-1}. We suggest that the difference could be explained by selection of the end-member in the mixing model, which has been previously described by others as a factor in correct determination of groundwater discharge (e.g. Peterson et al., 2008; Moore, 1996; Cerdà-Domènech et al., 2017). A critical component in any tracer study is the selection of a representative groundwater end-member (Ra_{SGD} and Sal_{SGD}) collected at the point of discharge.

All submarine springs described here are located in submarine caves (Cantarrijan, Palomas, and Sifon Caves) with vents parallel to the surface (i.e. horizontal geometry) at depths of 8 – 15 m below sea level. The springs discharge occurs parallel to the land surface at about 5 – 10 m landward from the caves entrance. SCUBA diving to the springs vents for representative groundwater/spring water end-member was challenging, thus the presented estimates of spring discharge are based on groundwater from the closest located well (GW-CG-1, Fig. 1) with a ^{224}Ra concentration of 1260 ± 90 dpm m^{-3} and salinity of 2.2 ± 0.1.

Because springs conduits are subject to seawater intrusion, we suggest that the salinity of the discharging spring water could be slightly to significantly higher than groundwater salinity sampled from the inland well (GW-CG-1) which we used as the groundwater end-member (Ra_{SGD} and Sal_{SGD}). While in fresh water, radium is mostly attached to particles and its dissolved concentration is very low, in brackish spring water radium would be mostly dissolved and we would have observed higher ^{224}Ra in the end-member waters (Burnett et al., 2006; Cerdà-Domènech et al., 2017). Based on the correlation between salinity and ^{224}Ra desorption, a salinity increase of 5 to the groundwater end-member (GW-CG-1) would produce an extrapolated ^{224}Ra increase of 60 dpm m^{-3}, resulting in a decrease spring flux of about 65%, which is closer to the salinity mass balance estimation. A salinity of 5 in submarine springs seems reasonable as it is similar to those found by García-Solsona et al. (2010) in a coastal karst

777 aquifer in eastern Spain, where annual average salinity of outflowing brackish submarine springs
778 was 6.8. Furthermore, in well GW-CG-1 located 500 m inland from the submarine springs in the
779 karstic marble, a salinity value of 2.2 was measured, also indicating that a value of 5 was
780 plausible.

781 The salinity mass balance method estimates only the fresh water fraction of the spring
782 discharge. In this way, the difference in discharge estimation using a ^{224}Ra and a salinity mass
783 balance is found because the ^{224}Ra method estimates the total (brackish) discharge, while the
784 salinity method accounts only for the fresh portion. Therefore, only the spring discharge based
785 on the salinity model should be used in the water budget of Sierra Almijara-Alberquillas Aquifer.

786 *Diffuse groundwater seepage through seabed sediments*: In contrast to the case of
787 submarine spring discharge, we found that groundwater seepage through seabed sediments
788 (Maro Cliff, conglomerate section; and Cantarrijan Beach, karst section) was most adequately
789 detectable using ^{222}Rn as a tracer and direct measurements (i.e. seepage meters). The
790 observed ^{222}Rn concentrations in receiving surface waters were as high as $44 \pm 3 \times 10^3$ dpm m^{-3}
791 at both groundwater seepage areas, i.e. Maro Cliff and Cantarrijan Beach (Fig. 4).

792 Although, we also observed high ^{224}Ra concentrations in samples collected near
793 Cantarrijan Beach (Fig. 3), these were associated with nearby discharge from the Cantarrijan
794 Caves submarine spring (Fig. 3, sampling points SW-6, SW-7, and SW-13). Indeed, during one
795 of the dry period sampling events (July of 2016), we did not detect any ^{224}Rn in coastal waters of
796 Cantarrijan Beach giving us confidence that the previously observed signals (September 2010)
797 were from the springs and not from the diffuse seepage. For the same reason, salinity could not
798 be used as a tracer in either of the seepage areas (Maro Cliff and Cantarrijan Beach) because

799 salinity anomalies were also created mostly by nearby coastal and submarine springs
800 respectively, overwhelming the salinity signal that is only due to diffuse seepage.

801 In this complex scenario, ^{222}Rn was the only groundwater tracer able to uniquely identify
802 diffuse groundwater seepage to the sea and a ^{222}Rn mass balance was thus used to quantify
803 groundwater seepage fluxes. Based on this mass balance in the Maro Cliff area, we calculated a
804 discharge of $2.9 \pm 0.8 \times 10^3$ m^3 d^{-1} (Table 2), whereas using seepage meter deployments (n = 4)
805 the discharge was $2.1 \pm 0.4 \times 10^3$ m^3 d^{-1}. In the Cantarrijan Beach we found very similar seepage
806 flux estimates using the ^{222}Rn approach ($0.9 \pm 0.1 \times 10^3$ m^3 d^{-1}) and using seepage meters ($0.8 \pm$
807 0.2×10^3 m^3 d^{-1}) with a total of 9 deployments (Table 2). While the two methods agree very well,
808 we recommend using the ^{222}Rn method over seepage meters. The main advantages of the ^{222}Rn
809 technique are (1) fully automatic data collection with very little field efforts, (2) temporal and
810 spatially integrated SGD estimates, which allow capturing small hydraulic conductivity
811 variations over large areas of diffuse seepage (Burnett et al., 2001).

812 *Subaerial forms of groundwater discharge to the sea (coastal springs and groundwater-*
813 *fed creeks)*: Coastal springs, and creeks that are primarily groundwater sustained, were only
814 present at the conglomerate and schist sections of the study site that are comprised of
815 conglomerate and schist, where permeablities are lower than in the marble formation (karst
816 section). During boat surveys ^{222}Rn activity levels in coastal waters of these two sections were
817 always within background offshore values ($1.0 \pm 0.2 \times 10^3$ dpm m^{-3}, Fig. 5) even at the points of
818 coastal springs and groundwater-fed creeks discharge that were visually identified. We attributed
819 the observed low ^{222}Rn concentrations to degassing and radioactive decay during groundwater
820 transit from land to the ocean. For instance, ^{222}Rn concentration at the point of the groundwater-
821 fed Maro Creek origin (Maro Spring, 250 ± 90 dpm m^{-3}) was significantly higher than at the

822 point of the Creek entrance to the sea (Maro Creek 3, 16 ± 7 dpm m^{-3}) (Fig. 1; Supplementary
823 material Table A.2). However, we were able to find groundwater signature of the Miel Creek and
824 the Alberquillas coastal spring in coastal waters of the schist section using ^{224}Ra concentration
825 anomalies; radium was 56 ± 4 dpm m^{-3} and 12 ± 2 dpm m^{-3} respectively at their point of entry to
826 the sea (Fig. 1). While coastal springs were easily located visually, additional field efforts were
827 usually required to determine whether the creeks were solely fed by groundwater inputs from the
828 karst aquifer in order to be considered (or not) in the total groundwater budget of Sierra
829 Almijara-Alberquillas Aquifer.

830 *Total groundwater discharge to Maro-Cerro Gordo coastal area:* Combining all
831 groundwater fluxes to the sea in Maro-Cerro Gordo, we estimate a daily groundwater discharge
832 that ranged between 9 ± 2 × 10^3 m^3 d^{-1} during dry periods and 12 ± 3 × 10^3 m^3 d^{-1} during wet
833 periods, with an average of 11 ± 3 × 10^3 m^3 d^{-1}. This combined discharge is composed of: 3.6 –
834 4.0 × 10^3 m^3 d^{-1} in the conglomerate section, 2.4 – 3.6 × 10^3 m^3 d^{-1} in the schist section , and 3.3 –
835 4.7 × 10^3 m^3 d^{-1} in the karst section (Supplementary material Table A.2). As described above,
836 differences in the geologic settings in each section, have defined the form of groundwater flow to
837 the sea (Fig. 10, Table 4).

838

839 **Figure 10: Total groundwater discharge (TGD) in the study area divided in forms of discharge (GS:**
840 **groundwater diffuse seepage, CS: coastal springs, GC: groundwater-fed creeks, SS: submarine**
841 **springs), showing maximum and minimum flux during wet and dry periods.**

842

843 In the conglomerate section, most of the groundwater flow takes place preferentially
844 through the travertine formation as groundwater seepage and it is 25 - 31% of the total discharge
845 in the study area, whereas small coastal springs dispersed along the section contribute to 5 – 6%,

and groundwater-fed creeks for 1 – 2%. The ubiquitous presence of a schist formation in the schist section impedes direct submarine flow and groundwater discharge converges in two points: groundwater-fed Miel Creek, and Alberquillas coastal spring which account for 25 – 30% of the total discharge. In the karst section, where Sierra Almijara-Alberquillas Aquifer is in direct connection with the sea, SGD takes place as groundwater seepage through marine sediments in Cantarrijan Beach assessed to account for 10 - 18%. Karstic submarine springs in Cantarrijan Caves, Palomas Cave, and Sifon Cave represent 19 - 25% of the total groundwater discharge to the sea.

5.2 Complexity of Sierra Almijara-Alberquillas karst aquifer hydrodynamics

The large spatial variations in the different forms of groundwater discharge in this coastal karst aquifer were also reflected in the seasonal variability of discharge during contrasting periods (Fig. 2). For instance, in Maro Cliff (conglomerate section, Fig. 1) we expected higher seepage rates in December during the wet period (Fig. 2). However, the discharge estimations for the dry period (July) and the wet period (December) were statistically identical: groundwater seepage in Maro Cliff during the dry period was $2.9 \pm 0.8 \times 10^3$ m^3 d^{-1} and $3.0 \pm 0.8 \times 10^3$ m^3 d^{-1}during the wet period.

There are two hypotheses that attempt to explain the observed lack of seasonal variation of groundwater discharge in Maro Cliff. The first hypothesis suggests that the observed steady flow is maintained by continuous infiltration of agricultural irrigation water used by the adjacent greenhouse fields. A second hypothesis, proposed by Espejo et al. (1988) and Castillo et al. (2001) suggests that the surplus of groundwater that maintains the base flow during the dry season originates from the Sierra Almijara-Alberquillas Aquifer. The authors propose that groundwater is transferred from the Sierra Almijara-Alberquillas Aquifer to the coast through the

adjacent conglomerate unit and travertines near the small town of Maro. These two hydrogeologic units are indeed in immidate contact with the sea (Fig. 1).To test both hypotheses we used two common geochemical approaches.

We first differentiated between heavier isotopic (δ^2H and $\delta^{18}O$) compositions (more positive values), associated with evaporation processes or mixing with seawater (Gat, 1971). The isotopic composition of groundwater collected from Maro Spring (i.e. in the conglomerate section) showed the most negative values (-46‰, -7.7‰) on the local groundwater line (LWL) in this area (Fig. 8b). These values correspond to the composition of deep groundwater flow in Sierra Almijara-Alberquillas Aquifer (Liñán et al., 2000). Groundwater seepage in Maro Cliff presents average isotopic values (-44‰ and -7.4‰) that are similar but slightly higher than Maro Spring, suggesting that water transfer from the marble formation is a plausible option.

To differentiate between irrigation water and water transferred from the Sierra Almijara-Alberquillas Aquifer to the travertines, the water stable isotopes end-members have to be very different than the deep/spring groundwater which has a negative composition compared to more positive values of evaporated irrigation water. We know that the water used for irrigation is withdrawn by farmers from Maro Spring. However, once extracted and in contact with the atmosphere, the water isotopic composition changes to more positive isotopic values. We also found that the collected spring water utilized for irrigation is typically stored in holding tanks and used when needed. During this holding time and in the process of irrigation, the water experiences further evaporation, and as a result, it should result in even more positive isotopic signature such us the waters of the coastal spring Barranco Maro (up to -43 and -7.3). The isotopic signature of irrigation water is thus, very different from the original Maro Spring water, allowing us to define a two-end-member system where coastal spring Huerto Romero represents

892 the most evaporated irrigation water (Fig. 8b). Based on a mixing model using these end-
893 members we found that seeping groundwater at Maro Cliff is indeed composed mostly from
894 infiltrating irrigation water. We also found that the ratio of Maro Spring water to irrigation
895 changes depending on the season with highest percentage (up to 82%) of irrigation water during
896 the dry period compared to the wet period (74%).

897 To further confirm these finding, we utilized water quality parameters, such as sulfate
898 (SO_4^{2-}) and nitrate (NO_3^-) concentrations, to differentiate between these two water sources.
899 Infiltrated irrigation water should have much higher NO_3^- concentrations and constant SO_4^{2-},
900 whereas deep groundwater should natural concentrations of NO_3^-. Thus, NO_3^- content can be
901 used as an indication of irrigation origin. The isotopic composition of Sierra Almijara-
902 Alberquillas Aquifer in this area fall within a narrow SO_4^{2-} concentration range (1700 – 2600
903 mmol m^{-3}) (Fig. 11), being naturally high in Maro Spring groundwater (Liñán et al., 2000).
904 When plotting SO_4^{2-} and NO_3^- concentrations in water, all water samples derived from Maro
905 Spring before infiltration showed low NO_3^- concentration (5 – 21 mmol m^{-3}) and naturally high
906 levels of SO_4^{2-} (Fig. 11). All samples collected from coastal springs that discharge to the sea
907 (Doncellas, Barranco Maro, Huerto Romero, and Maro Beach coastal springs), showed levels of
908 SO_4^{-2} typical of Sierra Almijara-Alberquillas Aquifer and high levels of NO_3^- (more than 350
909 mmol m^{-3}) indicating fertilizer inputs. On the other hand, samples collected at the area of
910 seepage through seabed sediments in the Maro Cliff, showed NO_3^- concentrations (130 mmol m^{-3})
911 that are closer to the observed background levels of Sierra Almijara-Alberquillas groundwater
912 representative (5 – 21 mmol m^{-3}) than to the contaminated infiltrated water (Fig. 11).
913
914 **Figure 11: Groundwater ionic relationship between NO_3^- and SO_4^{2-} where groundwater samples**
915 **with similar composition are grouped in dashed squares. Symbols are presented as in Fig. 8 based**

on the section and lithology they are located. In the conglomerate section Maro Spring, Nerja Cave, and Maro Creek show similar SO_4^{2-} concentration with low NO_3^-, while Doncellas, Barranco Maro, Huerto Romero, and Maro Beach present NO_3^- contamination. Samples from the schist section (Miel and Alberquillas) present a distinctive signal with low NO_3^- and SO_4^{2-} concentrations. Groundwater collected in Cantarrijan Beach (karst section) shows seawater influence from saltwater recirculation in beach sediments. Arrows indicate the geochemical change before irrigation and after fertilizers application (NO_3^-), where Maro cliff (diffuse seepage) shows mixing between both groups.

Therefore, we are confident that groundwater seepage to the sea observed and quantified in Maro Cliff is mostly generated as a result of infiltrated irrigation water. We found uniform groundwater flux (independently of rainfall) in this area throughout the year (Fig. 6a) supporting this hypothesis. Irrigation occurs constantly throughout the year, and infiltration through the highly porous travertine constitutes a constant source of water that flows towards the coast and ultimately discharges into the sea as groundwater seepage. Irrigation water from greenhouse farming is collected from the Maro Spring and thus SGD in the Maro Cliff should not be added to the total budget of the aquifer system as it has been already accounted as groundwater from Maro Spring on land. This is a significant new finding and should be considered when compiling the total water budget of the Sierra Almijara-Alberquillas Aquifer.

In contrast to the groundwater seepage dynamics in Maro Cliff (conglomerate section), the seepage rates in the Cantarrijan Beach (karst section) were seasonally modulated; the groundwater flux that the Cantarrijan Beach area received in the dry period was $0.9 \pm 0.1 \times 10^3$ m^3 d^{-1} which was half of its wet period discharge ($2.3 \pm 0.3 \times 10^3$ m^3 d^{-1}). Differences in aquifer recharge and sea level variations between the dry and wet periods have control on the

940 magnitude of SGD (Carrasco et al, 1998; Santos et al., 2009). During dry periods precipitation
941 was absent for up to two months, decreasing the recharge from infiltrated meteoric water in
942 Sierra Almijara-Alberquillas Aquifer. Although during December of 2015 the area did not
943 receive any rainfall, rain events occurred during September-November contributed to the
944 recharge of Sierra Almijara-Alberquillas Aquifer, deriving in higher seepage fluxes in
945 Cantarrijan Beach (Fig. 2). Additionally, the mean sea level measured during 2010-2016 near the
946 study area (Permanent Service for Mean Sea Level,
947 http://www.psmsl.org/data/obtaining/stations/1940.php) showed seasonal fluctuations, with
948 lower sea levels during January-May compared to higher levels during August-December (Fig.
949 2). The observed moderate increase of 15 cm during the dry periods has contributed to the
950 observed higher salinity of groundwater in Cantarrijan Beach, as well as the overall lower
951 groundwater seepage rates during the dry periods.

952 Based on the salinity mixing model (Eqs. 9 and 10), we calculated that the fresh fraction
953 of SGD was 48% of the total groundwater seepage, which means that during July of 2016, only
954 $0.4 \pm 0.1 \times 10^3$ m^3 d^{-1} should be taken into account as part of the Sierra Almijara-Alberquillas
955 Aquifer water budget.

956 The salinity gradient observed from GW-Well to GW-Pz-4 is an indication that there is
957 saltwater recirculation in the beach sediments and with the ^{222}Rn approach we have captured
958 both the fresh and recirculated SGD (Fig. 6c). We did not repeat these measurements during the
959 wet period, but we can hypothesize that this percentage was very similar based on the salinity
960 measured in GW-Well during December of 2015 (Supplementary material Table A.2).

961 **5.3 Importance of groundwater discharge for the water budget of Sierra Almijara-**
962 **Alberquillas Aquifer and nitrate loading to Maro-Cerro Gordo coastal area**

963 To estimate the portion of the annual fresh groundwater discharge to the sea from Sierra
964 Almijara-Alberquillas Aquifer water budget, we extrapolated average daily fluxes to obtain an
965 annual range for the wet and dry periods (Table 4). During this study, we found that the total
966 groundwater discharge to the sea was $1.9 \pm 0.5 \times 10^6$ m^3 y^{-1} during the dry period, and $2.6 \pm 0.8 \times$
967 10^6 m^3 y^{-1} wet period (Table 4). Based on Pérez-Ramos and Andreo (2007) and Castillo et al.
968 (2001) the total annual groundwater budget of the Sierra Almijara-Alberquillas Aquifer is $50 \times$
969 10^6 m^3 y^{-1}, and thus the flux we estimated represents 4 - 5% of the water resources of this karst
970 system. This is a conservative estimate and should be considered as groundwater flow at base
971 conditions because sampling campaigns were purposely not conducted after big rain events (Fig.
972 2).

973 In these calculations, we do not account for groundwater seepage in Maro Cliff
974 (conglomerate section), coastal springs Doncellas, Barranco Maro, Huerto Romero, and Maro
975 Beach, and groundwater-fed Tierras Nuevas Creek as they are originated from irrigation water
976 that has been already accounted as outputs from Maro Spring.

977 Based on the groundwater discharge to the sea, NO_3^- fluxes per unit of shore length in the
978 conglomerate section were 205 ± 90 mmol m^{-1} d^{-1}, while the schist and karst sections together
979 receive between 15 ± 3 mmol m^{-1} d^{-1} on average. When normalized by shore length, NO_3^-
980 discharge in the conglomerate section is 3.5 mmol m^{-2} d^-, which compared to other
981 anthropogenically impacted sites of coastal karst aquifers in the Mediterranean, is very similar.
982 For example, García-Solsona et al. (2010) estimated a nitrate flux of 8.3 – 1.5 mmol m^{-2} d^{-1} in
983 eastern Spain, and Rodellas et al. (2014) found 0.97 mmol m^{-2} d^{-1} in Majorca Island (Balearic
984 Islands), whereas in a site in Menorca Island the flux was 18 mmol m^{-2} d^{-1} (García-Solsona et al.,
985 2010b). It is important to note that while it only represents 20% (or 3 km) of the total shoreline

length (16 km), the conglomerate section receives about 75% of the total NO_3^- delivered to Maro-Cerro Gordo coastal waters (Supplementary material Table A.2).

Since 1989 the Maro-Cerro Gordo Natural Area (schist and karst sections), has been protected due to the presence of endemic and endangered flora and fauna by the Council of Environment of Andalusia. The European Commission designated the area as a Special Protection Area (SPA), Specially Protected Area of Mediterranean Importance (SPAMI), Site of Community Importance (SCI), and Special Area of Conservation (SAC) (Aranda and Otero, 2014). Specifically, the conservation area hosts three species of marine phanerogams (*Zostera marina, Posidonia oceanica*, and *Cymodocea nodosa*), included in the IUCN Red List of Threatened Species. Seagrass provides a unique habitat for a wide range of species (Hughes et al., 2009); including the largest bivalve in the Mediterranean *Pinna nobilis* (Theodorou et al., 2015), endangered fish *Epinephelus marginatus* (Gallego et al., 2015), and marine turtle *Caretta caretta* (Tomas et al., 2001) among others. As other studies have demonstrated, nitrate surplus loading often alters the primary producers community (Rapport and Whitford, 1999), and fast growing micro and macroalgae can proliferate preventing seagrasses *Zostera marina* and *Posidonia oceanica* from having enough sunlight and space (Hauxwell et al., 2001; Deegan et al., 2002). For example, Valiela et al. (2002) demonstrated that seagrass production could decrease up to 90% when nitrogen inputs are higher than 500 kg N ha^{-1} y^{-1}. Only in the groundwater seepage area of Maro Cliff we have found that nitrogen fluxes (as nitrate) was about 2500 kg N ha^{-1} y^{-1}, which is five times higher than the Valiela et al.'s assessment and should be a major concern for the ecological status of the marine system in the conglomerate section (Fig. 1). However, to further understand the implications of nutrients fluxes to the sea on

1008 the marine ecosystem (particularly on endemic seagrass and fauna), additional investigation in
1009 the area must be conducted.

1010 **5.4 Sensitivity analysis of methods applied**

1011 To further compare the applicability of methodologies utilized in the presented multi-
1012 method approach, we constructed a sensitivity analysis including each method's main
1013 assumptions.

1014 **5.4.1 Parameter sensitivity of ^{224}Ra and salinity mass balance methods for**
1015 **determining discharge of submarine springs**

1016 Three terms represent the major source of uncertainty in the ^{224}Ra and salinity mass
1017 balances we used to calculate submarine spring discharge, including (1) the residence time of the
1018 receiving coastal waters (t), (2) the volume of the SGD plume (V), and (3) the uncertainty in the
1019 determination of groundwater end-member (Ra_{SGD}) (Table 5).

1020 The largest uncertainty in this model is given by the assumption of a one day residence
1021 time (t). A common technique for assessing water ages of coastal waters is based on short-lived
1022 radium isotopes, ^{223}Ra and ^{224}Ra (Moore, 2000). However, during this study we could not
1023 measure both radium isotopes and we were unable to apply this method. The karst section of
1024 Maro-Cerro Gordo displays rocky cliff areas spread across the geographically exposed to
1025 prevailing west winds coastline which reflects the influence of high energy waves. The karst
1026 aquifer has very high secondary porosity and permeability which provides the opportunity for
1027 extensive groundwater-surface water exchange. The estimate of a one day residence time for this
1028 study is based on a comparison to similar high-energy coastal environments that are typical for
1029 the Mediterranean coastline. Under similar hydrogeological conditions in eastern Spain, using
1030 the methodology presented in Moore (2000), García-Solsona et al. (2010) assessed residence

1031 time (*t*) between 1.1 d and 2.7 d, whereas Tovar-Sánchez et al. (2014) found residence times of
1032 1.7, and 1.2 days in three coves in a karst system in the eastern shore of the Majorca Island.
1033 Considering these studies and specifics of this study site, we suggest using residence times of
1034 0.25, 0.5, 1.0, and 3.0 days in the sensitivity analysis.

1035 To determine the volume (V = plume area × depth) of the SGD plume, we used areas of
1036 salinity sea surface anomalies created by the submarine springs discharge at Maro-Cerro Gordo.
1037 Specifically, we utilized salinity anomalies of -0.3, 0.0, 0.3, and 0.6 isolines. For vertical scale
1038 we use water depths acquired from the bathymetry database of the Andalusia Council of
1039 Environment (http://www.juntadeandalucia.es/medioambiente/site/rediam) assuming a well-
1040 mixed water column. However, Garcia-Solsona et al. (2010) found in eastern Spain that although
1041 complete mixing in the water column could be found near the karst springs vents, the salinity
1042 anomaly measured in surface waters was limited to the 0.5 m upper most layer. Similar settings
1043 are possible in Maro-Cerro Gordo; thus, we also calculated *V* based on the 0.0 salinity anomaly
1044 isoline and considering a depth of 0.5 m (Table 5)

1045 There are only two groundwater wells in the karst section of Maro-Cerro Gordo, (GW-
1046 CG-1 and GW-CG-2). For the sensitivity analysis we used ^{224}Ra concentration in GW-CG-1
1047 (1260 ± 90 dpm m^{-3}) and GW-CG-2 (1020 ± 80 dpm m^{-3}) as end-members, both sampled in
1048 September of 2006.

1049 After tabulating these parameters, both the ^{224}Ra and salinity mass balance models
1050 showed the highest sensitivity to variations in the volume affected by SGD (*V*). We found that
1051 the total discharge from submarine springs decreases by 80% when using salinity isolines of 0.6
1052 to -0.3 in a well-mixed water column; however, if the fresh plume is limited to the 0.5 m top
1053 layer of the water column, the decrease is up to 97%. Residence time (*t*) was the second most

important variable affecting the variability of discharge from submarine springs, increasing by 92% when changing the residence time from 0.25 to 3.0 days (Table 5). The ^{224}Ra mass balance showed limited sensitivity to varying groundwater end-member values (Ra_{SGD}), when using the GW-CG-2 value instead of GW-CG-1, all estimations increased only by 20%. The maximum variation utilizing the three variables simultaneously in the ^{224}Ra mass balance was 100% with a total discharge of 0.2 – 90.5 × 10^3 m^3 d^{-1}. The salinity mass balance presented a total variation of 100% to changing *t* and *V*, with a total discharge of 0.03 – 13.5 × 10^3 m^3 d^{-1}, which represents the purely fresh discharge (Table 5).

5.4.2 Parameter sensitivity of the ^{222}Rn mass balance and seepage meters measurements in determining diffuse seepage

In the ^{222}Rn model, we considered that only the seepage area (*A*) could be subject to ambiguity because all terms in the model (including the groundwater end-member) have been carefully measured. To delineate the size of the seepage face we used the following ^{222}Rn concentration isolines: for the Cantarrijan Beach we used the 10, 8, 6, and 5 dpm m^{-3}, while in Maro Cliff we used the 25, 30, 35, and 45 dpm m^{-3} (Table 5). For comparison reasons, were used the same seepage areas to calculate SGD when using the seepage meters approach. Using the 25 × 10^3 dpm m^{-3} ^{222}Rn concentration isoline in Maro Cliff produces 86% higher for both dry and wet periods, compared to seepage area based on the 45 × 10^3 dpm m^{-3} isoline. The discharge ranged from 0.9 – 6.7 × 10^3 m^3 d^{-1} and 0.9 – 7.5 × 10^3 m^3 d^{-1} during dry and wet periods respectively. In Cantarrijan Beach we found an increase of 82%, with a discharge estimation that ranged between 0.2 – 1.2 × 10^3 m^3 d^{-1} and 0.5 – 2.9 × 10^3 m^3 d^{-1} during dry and wet periods. The radon method showed higher sensitivity (89%) than the seepage meter assessments (87%) (Table 5).

5.4.3 Implications for the water budget of Sierra Almijara-Alberquillas Aquifer

Using the presented ranges of fluxes of each methodology, we calculated a total groundwater discharge to the sea of 4.3 – 105.1 × 10^3 m^3 d^{-1} from all forms of discharge (Table 6). The fresh water component of the total discharge can be obtained from the salinity mass balance in submarine springs, ^{222}Rn mass balance and seepage meters for diffuse seepage in Cantarrijan Beach (47% fresh, based on the salinity mixing model), Caleta and Miel Creeks, and Alberquillas Spring (see sections 5.2 and 5.3). Applying a residence time of 0.25 d, the lowest estimated volumes affected by the SGD plume (*V*) at each submarine spring (0.2 × 10^5 m^3, 0.18 × 10^5 m^3, 0.19 × 10^5 m^3) derived from a 0.5 m water column, and the largest estimates for seepage face in Cantarrijan Beach (A = 1.0 × 10^3 m^2) for the ^{222}Rn model and seepage meter methods, the minimum fresh groundwater discharge is 0.9 × 10^6 m^3 y^{-1}. Applying the assumption of a 3-days residence time, the largest *V* at each submarine spring (4.6 × 10^5 m^3, 8.7 × 10^5 m^3, 7.1 × 10^5 m^3), and the largest *A* in cantarrijan Beach (5.7 × 10^3 m^2) for the ^{222}Rn model and seepage meter methods, the maximum fresh groundwater discharge from Sierra Almijara-Alberquillas Aquifer is 6.8 × 10^6 m^3 y^{-1}. A total groundwater discharge of 6.8 × 10^6 m^3 y^{-1} seems plausible but unlikely during base flow conditions when compared to the total water budget of Sierra Almijara-Alberquillas (50 × 10^6 m^3 y^{-1}). However, a residence time of 1 day seems more realistic based on other studies conducted in similar areas. The application of this sensitivity analysis including all terms and applying a 1-day residence time gives a total discharge of 1.0 – 3.5 × 10^6 m^3 y^{-1}.

5.5 Global applicability of the presented methodology approach

The modes of discharge found in Maro-Cerro Gordo are commonly observed in other areas worldwide independent of climate. About half of the Mediterranean and Adriatic coastline is comprised of karst aquifers and hydrogeological settings similar to Maro-Cerro Gordo can be expected (Fleury et al., 2007, 2005; Surić et al., 2015). In most scenarios authors often point out that groundwater discharge was not quantified due to the complex settings where at least two forms of discharge occur in multiple locations (e.g. Fleury et al., 2007; Burnett et al., 2008). Similar problems are encountered in karst coastlines in the Yucatan Peninsula (Mexico), a karst platform located in the Caribbean Sea. Gonneea et al. (2014) assumed that submarine springs were representative of the total SGD in the study area, but pointed out that diffuse discharge away from springs was not measured. Null et al. (2014) assessed SGD in the eastern shore of the Yucatan Peninsula where submarine springs and diffuse seepage are present. Due to the lack of a field method to quantify groundwater seepage, they used analytical calculations to establish a first order approximation of SGD. Furthermore, SGD in volcanic systems, although geologically different than karst, have comparable dynamics due to the similar intrinsic porosity and permeability (Burnett et al, 2008; Johnson et al., 2008; Peterson et al, 2009, Dimova et al, 2012).

Common characteristics of these sites include (1) simultaneous groundwater discharge to the sea occurring in two or more forms due to highly heterogeneous geological settings, (2) high infiltration rates resulting in negligible riverine freshwater inputs, and (3) significant groundwater inputs.

6 Conclusions

Work presented here demonstrates that determining total groundwater discharge to the ocean from coastal karst aquifers is not trivial and it requires a very good understanding of the

1122 geology and groundwater origin to constrain an adequate water budget. Specifically, as a result
1123 of the complex geology of Maro-Cerro Gordo coastal area and highly heterogeneous Sierra
1124 Almijara-Alberquillas coastal karst aquifer, we found that groundwater discharge manifests in
1125 four different forms: (1) groundwater-fed creeks, (2) coastal springs, (3) groundwater seepage
1126 through seabed sediments, and (4) submarine springs. These expressions of discharge are typical
1127 for karst systems and should be expected in similar geological settings elsewhere including
1128 volcanic systems, which although having different rock composition, behave hydrologically very
1129 similar. We found that only the application of a set of methods specific for each form of
1130 discharge adequately characterizes and gives a realistic evaluation of groundwater discharge to
1131 the sea and thus recommend the following approaches (Table 6).

1132 Continuous ^{222}Rn measurements in coastal waters via boat surveys proved to be the most
1133 reliable method for detecting diffuse groundwater seepage through seabed sediments. The
1134 technique complements well with a ^{222}Rn mass balance model based on time-series
1135 measurements performed with the same instrumentation. We found that this method gives
1136 similar results to direct measurements carried out from Lee-type seepage meters.

1137 The presence of submarine springs was reliably detected using continuous salinity
1138 measurements and discreet ^{224}Ra sampling. However, because negative salinity anomalies in
1139 coastal waters could be the result of discharge of other freshwater inputs (e.g. groundwater-fed
1140 creeks and coastal springs) which are likely to occur in karst systems, salinity alone is not a
1141 reliable tracer for SGD in coastal karst systems. We were able to confirm the presence of
1142 submerged springs only when combined with high concentrations of ^{224}Ra concentrations and
1143 direct observations via SCUBA diving. Direct flowmeter measurements or applying the ^{222}Rn

method would have been technically and economically challenging, given the springs depth and their lateral vent geometry.

Subaerial coastal springs and groundwater-fed creeks are easily detectable visually in the field. However, we found that tracer surveys are helpful to identify sources of springs and assessing the total discharge from both forms of subaerial groundwater discharge.

We found that the combination of hydrochemistry (SO_4^{-2} and NO_3^-) and water stable isotopes (δ^2H and $\delta^{18}O$) was ideal to decipher the origin of each point of groundwater discharge to the sea.

Nitrate fluxes, in an area where endemic and protected seagrasses *Zostera marina, Posidonia oceanica* are present, were found to be comparable with other coastal karst aquifers environmentally impacted by anthropogenic activities in the Mediterranean.

Based on our experience, we strongly recommend the application of the described methodology approach in coastal karst systems to assess total groundwater discharge to the sea and associated nutrients fluxes.

Acknowledgments

This research was partially funded by the University of Alabama Graduate School Research and Travel Support Fund, the UA Department of Geological Sciences W. Gary Hooks Geological Sciences Advisory Board Fund, and the A.S. Johnson Travel Fund. This work is a contribution to the Research Group RNM-308 of the Junta de Andalucía, and CGL2015-65858-R of DGICYT. V.R. acknowledges support from the European Union's Horizon 2020 research and innovation program under the Marie Skłodowska-Curie grant agreement No 748896. J.G.O would like to thank the support of the Generalitat de Catalunya to MERS (2014 SGR – 1356). We would also

want to thank José Antonio Espejel Carrión, Guillermo González Lozano, Javier López-Murcia Martin, Matías Mudarra Martínez, Diego Naranjo Roldán Fernando Nuño López, and Juan Manuel Ruiz for their extensive help in the field.

References

Andreo, B., Carrasco, F., Sanz de Galdeano, C., 1993. Estudio geológico del entorno de la Cueva de Nerja. Geología de la Cueva de Nerja, 3, 25-50.

Andreo, B., Carrasco, F., 1993. Estudio hidrogeológico del entorno de la Cueva de Nerja. Trabajos Cueva Nerja, 3, 163-187.

Andreo, B., Vías, J., Durán, J. J., Jiménez, P., López-Geta, J. A., Carrasco, F., 2008. Methodology for groundwater recharge assessment in carbonate aquifers: application to pilot sites in southern Spain. Hydrogeology Journal, 16, 911-925.

Andreo, B., Barberá, J. A., Mudarra, M., Marín, A. I., García-Orellana, J., Rodellas, V., Pérez, I., 2017. A multi-method approach for groundwater resource assessment in coastal carbonate (karst) aquifers: the case study of Sierra Almijara (southern Spain). Hydrogeology Journal, 1-16.

American Public Health Association (APHA), American Water Works Association (AWWA), and Water Environment Federation (WEF), 1999. In Clescerl L., Greenberg A., Eaton A. (Eds), Standard Methods for the Examination of Water and Wastewater 20th Edition. United Book Press, Inc., Baltimore, Maryland. Part 2000, pp. 2-48.

Aranda, Y., Otero, M., 2014. Estudio de las figuras de protección de áreas marinas protegidas de Andalucía con fanerógamas marinas y propuestas de mejora para su gestión. Anexo VI. LIC

1188 Arfib, B., Charlier, J. B., 2016. Insights into saline intrusion and freshwater resources in coastal
1189 karstic aquifers using a lumped Rainfall–Discharge–Salinity model (the Port-Miou brackish
1190 spring, SE France). Journal of Hydrology, 540, 148-161.

1191 Aunay, B., le Strat, P., Duvail, C., Dörfliger, N., Ladouche, B., 2003. Méthode d'analyse
1192 géologique sur la karstification des Corbières orientales et influence des évènements néogènes
1193 (tortono-messiniens). Hydrology of the Mediterranean and Semiarid Regions. IAHS,
1194 Montpellier, (278), 124-129

1195 Bakalowicz, M., 2005. Karst groundwater: a challenge for new resources. Hydrogeology Journal,
1196 13, 148-160.

1197 Bakalowicz, M., El Hakim, M., El-Hajj, A., 2008. Karst groundwater resources in the countries
1198 of eastern Mediterranean: the example of Lebanon. Environmental Geology, 54, 597-604.

1199 Bakalowicz, M., 2015. Karst and karst groundwater resources in the Mediterranean.
1200 Environmental Earth Sciences, 74, 5-14.

1201 Bañares-España E., Báez J.C., Casado M.D., Díaz de Rada C., Flores-Moya A., Rey J., 2002.
1202 Distribución y estado de las fanerógamas marinas en el Paraje natural Acantilados de Maro-
1203 Cerro gordo (Málaga-Granada). García-Gómez J.C., Finlayson C. (Eds.), Libro de Resúmenes,
1204 XII Simposio Ibérico del Bentos Marino, Impresur, Algeciras, 30–31.

1205 Barberá, J. A., Andreo, B., 2015. Hydrogeological processes in a fluviokarstic area inferred from
1206 the analysis of natural hydrogeochemical tracers. The case study of eastern Serranía de Ronda (S
1207 Spain). Journal of Hydrology, 523, 500-514.

1208 Benac, Č., Rubinić, J., Ožanić, N., 2003. The origine and evolution of coastal and submarine
1209 springs in Bakar Bay. Acta Carsologica, 32, 157-171.

1210 Bonacci, O., Roje-Bonacci, T., 1997. Sea water intrusion in coastal karst springs: example of the
1211 Blaž Spring (Croatia). Hydrological Sciences Journal, 42, 89-100.

1212 Burnett, W. C., Taniguchi, M., Oberdorfer, J., 2001. Measurement and significance of the direct
1213 discharge of groundwater into the coastal zone. Journal of Sea Research, 46, 109-116.

1214 Burnett, W. C., Dulaiova, H., 2003. Estimating the dynamics of groundwater input into the
1215 coastal zone via continuous radon-222 measurements. Journal of Environmental Radioactivity,
1216 69, 21-35.

1217 Burnett, W. C., Bokuniewicz, H., Huettel, M., Moore, W. S., Taniguchi, M., 2003. Groundwater
1218 and pore water inputs to the coastal zone. Biogeochemistry, 66, 3-33.

1219 Burnett, W. C., Aggarwal, P. K., Aureli, A., Bokuniewicz, H., Cable, J. E., Charette, M. A.,
1220 Kontar, E., Krupa, S., Kulkarni, K.M., Loveless, A., Moore, W. S., 2006. Quantifying
1221 submarine groundwater discharge in the coastal zone via multiple methods. Science of the Total
1222 Environment, 367, 498-543.

1223 Burnett, W. C., Santos, I. R., Weinstein, Y., Swarzenski, P. W., Herut, B., 2007. Remaining
1224 uncertainties in the use of Rn-222 as a quantitative tracer of submarine groundwater discharge. A
1225 New Focus on Groundwater–Seawater Interactions (Proceedings of Symposium HS1001 at
1226 IUGG2007, Perugia, July 2007. IAHS publication, 312, 109.

1227 Burnett, W. C., Peterson, R., Moore, W. S., de Oliveira, J., 2008. Radon and radium isotopes as
1228 tracers of submarine groundwater discharge–results from the Ubatuba, Brazil SGD assessment
1229 intercomparison. Estuarine, Coastal and Shelf Science, 76, 501-511.

1230 Butscher, C., Huggenberger, P., 2007. Implications for karst hydrology from 3D geological
1231 modeling using the aquifer base gradient approach. Journal of hydrology, 342, 184-198.

1232 Cable, J. E., Burnett, W. C., Chanton, J. P., Weatherly, G. L., 1996. Estimating groundwater
1233 discharge into the northeastern Gulf of Mexico using radon-222. Earth and Planetary Science
1234 Letters, 144, 591-604.

1235 Carrasco, F., Durán, J. J., Andreo, B., Liñán, C., Vadillo, I., 1998. Consideraciones sobre el karst
1236 de Nerja. Karst en Andalucia, 173-181.

1237 Castillo, A., Carmona, J., Benavente Herrera, J., 2001. Cuantificación de los recursos hídricos en
1238 la vertiente meridional del Parque Natural de Sierra Almijara (Málaga). Consideraciones sobre
1239 su régimen de explotación. Geogaceta 29, 33-36.

1240 Cerdà-Domènech, M., Rodellas, V., Folch, A., García-Orellana, J., 2017. Constraining the
1241 temporal variations of Ra isotopes and Rn in the groundwater end-member: Implications for
1242 derived SGD estimates. Science of the Total Environment, 595, 849-857.

1243 Charette, M. A., Buesseler, K. O., Andrews, J. E., 2001. Utility of radium isotopes for evaluating
1244 the input and transport of groundwater-derived nitrogen to a Cape Cod estuary. Limnology and
1245 Oceanography, 46, 465-470.

1246 Charette, M. A., 2007. Hydrologic forcing of submarine groundwater discharge: Insight from a
1247 seasonal study of radium isotopes in a groundwater-dominated salt marsh estuary. Limnology
1248 and Oceanography, 52, 230-239.

1249 Cockenpot, S., Claude, C., Radakovitch, O., 2015. Estimation of air–water gas exchange
1250 coefficient in a shallow lagoon based on ^{222}Rn mass balance. Journal of Environmental
1251 Radioactivity, 143, 58-69.

1252 Corbett, D., Burnett, W., Cable, P., Clark, S., 1998. A multiple approach to the determination of
1253 radon fluxes from sediments. Journal of Radioanalytical and Nuclear Chemistry, 236, 247-253.

1254 Craig, H., 1961. Isotopic variations in meteoric waters. Science, 133, 1702-1703

1255 Crusius, J., Koopmans, D., Bratton, J. F., Charette, M. A., Kroeger, K., Henderson, P., Ryckman,
1256 L., Halloran, K. Colman, J. A., 2005. Submarine groundwater discharge to a small estuary
1257 estimated from radon and salinity measurements and a box model. Biogeosciences, 2, 141-157.

1258 Custodio, E., 2010. Coastal aquifers of Europe: an overview. Hydrogeology Journal, 18, 269-
1259 280.

1260 Deegan, L. A., Wright, A., Ayvazian, S. G., Finn, J. T., Golden, H., Merson, R. R., Harrison, J.,
1261 2002. Nitrogen loading alters seagrass ecosystem structure and support of higher trophic levels.
1262 Aquatic Conservation: Marine and Freshwater Ecosystems, 12, 193-212.

1263 Dimova, N., Burnett, W. C., Lane-Smith, D., 2009. Improved automated analysis of radon
1264 (^{222}Rn) and thoron (^{220}Rn) in natural waters. Environmental Science & Technology, 43, 8599-
1265 8603.

1266 Dimova, N. T., Burnett, W. C., Speer, K., 2011. A natural tracer investigation of the hydrological
1267 regime of Spring Creek Springs, the largest submarine spring system in Florida. Continental
1268 Shelf Research, 31, 731-738.

1269 Dimova, N. T., Swarzenski, P. W., Dulaiova, H., Glenn, C. R., 2012. Utilizing multichannel
1270 electrical resistivity methods to examine the dynamics of the fresh water–seawater interface in
1271 two Hawaiian groundwater systems. Journal of Geophysical Research: Oceans, 117, C02012, 1-
1272 12.

1273 Dimova, N. T., Paytan, A., Kessler, J. D., Sparrow, K. J., García-Tigreros Kodovska, F., Lecher,
1274 A. L., Murray, J. Tulaczyk, S. M., 2015. Current magnitude and mechanisms of groundwater
1275 discharge in the Arctic: case study from Alaska. Environmental Science & Technology, 49,
1276 12036-12043.

1277 Dulaiova, H., Peterson, R., Burnett, W.C., Lane-Smith, D., 2005. A multi-detector continuous
1278 monitor for assessment of ^{222}Rn in the coastal ocean. Journal of Radioanalytical and Nuclear
1279 Chemistry, 263 , 361-365.

1280 Dulaiova, H., Burnett, W. C., 2006. Radon loss across the water-air interface (Gulf of Thailand)
1281 estimated experimentally from ^{222}Rn-^{224}Ra. Geophysical Research Letters, 33, L05606, 1-4.

1282 Durán, J. J., 1996. Los sistemas kársticos de la provincia de Málaga y su evolución. Contribución
1283 al conocimiento paleoclimático del Cuaternario en el Mediterráneo Occidental (Ph.D.
1284 Dissertation). Universidad Complutense de Madrid, Madrid, 409 p.

1285 Espejo, J.M., Luanco M. C., Linares L., 1988. Inventario de surgencias de aguas de origen
1286 continental en el litoral mediterráneo del sur de España, mediante utilización de sensores

1287 térmicos aeroportados con apoyo de técnicas oceanográficas e hidrogeológicas. In: Fernández-
1288 Rubio, R., López-Geta, J. A., Ramos-González, G. (Eds.), Tecnología de la Intrusión en
1289 Acuiferos Costeros. TIAC'88, IGME, Madrid, pp. 191-228.

1290 Fleury, P., 2005. Sources sous-marines et aquifères karstiques côtiers méditerranéens.
1291 Fonctionnement et caractérisation. PhD dissertation, Université Paris VI, 286 p.

1292 Fleury, P., Bakalowicz, M., de Marsily, G., 2007. Submarine springs and coastal karst aquifers: a
1293 review. Journal of Hydrology, 339, 79-92.

1294 Fourniguet, J., 1975. Néotectonique et Quaternaire marin sur le littoral de la Sierra Nevada,
1295 Andalousie (Espagne). PhD dissertation. University of Orléans, 234 p.

1296 Gallego, M. A. B., Reyes, O. M., 2015. La población de meros Epinephelus marginatus en el
1297 litoral andaluz (España). Chronica Naturae, 5, 68-80.

1298 García-Solsona, E., García-Orellana, J., Masqué, P., Dulaiova, H., 2008. Uncertainties associated
1299 with 223 Ra and 224 Ra measurements in water via a Delayed Coincidence Counter (RaDeCC).
1300 Marine Chemistry, 109, 198-219.

1301 García-Solsona, E., García-Orellana, J., Masqué, P., Rodellas, V., Mejías, M., Ballesteros, B.,
1302 Domínguez, J. A., 2010. Groundwater and nutrient discharge through karstic coastal springs
1303 (Castelló, Spain). Biogeosciences, 7, 2625-2638.

1304 García-Solsona, E., García-Orellana, J., Masqué, P., Garcés, E., Radakovitch, O., Mayer, A.,
1305 Estradé, S Basterretxea, G., 2010. An assessment of karstic submarine groundwater and
1306 associated nutrient discharge to a Mediterranean coastal area (Balearic Islands, Spain) using
1307 radium isotopes. Biogeochemistry, 97, 211-229.

1308 Gat, J.R., Garmi, I., 1970: Evolution of the isotopic composition of atmospheric waters in the
1309 Mediterranean Sea area. Journal of Geophysical Research., 75, 3039 – 3048.

1310 Gat, J. R., 1971. Comments on the stable isotope method in regional groundwater investigations.
1311 Water Resources Research, 7, 980-993.

1312 Gonneea, M. E., Charette, M. A., Liu, Q., Herrera-Silveira, J. A., Morales-Ojeda, S. M., 2014.
1313 Trace element geochemistry of groundwater in a karst subterranean estuary (Yucatan Peninsula,
1314 Mexico). Geochimica et Cosmochimica Acta, 132, 31-49.

1315 Guerra-Merchán, A., Serrano, F., 1993. Análisis estratigráfico de los materiales neógeno-
1316 cuaternarios de la región de Nerja. Geología de la Cueva de Nerja, 3, 53-90.

1317 Hallegraeff, G. M., 1993. A review of harmful algal blooms and their apparent global increase.
1318 Phycologia, 32, 79-99.

1319 Hauxwell, J., Cebrián, J., Furlong, C., Valiela, I., 2001. Macroalgal canopies contribute to
1320 eelgrass (Zostera marina) decline in temperate estuarine ecosystems. Ecology, 82, 1007-1022.

1321 Hughes, A. R., Williams, S. L., Duarte, C. M., Heck, K. L., Waycott, M., 2009. Associations of
1322 concern: declining seagrasses and threatened dependent species. Frontiers in Ecology and the
1323 Environment, 7, 242-246.

1324 Isiorho, S. A., Meyer, J. H., 1999. The effects of bag type and meter size on seepage meter
1325 measurements. Ground Water, 37, 411-413.

1326 Johnson, A. G., Glenn, C. R., Burnett, W. C., Peterson, R. N., Lucey, P. G., 2008. Aerial infrared
1327 imaging reveals large nutrient-rich groundwater inputs to the ocean. Geophysical Research
1328 Letters, 35, L15606, 1-6.

1329 Johnson, A. G. (2008). Groundwater discharge from the leeward half of the Big Island, Hawai‘i.
1330 PhD dissertation. University of Hawai’I, 145 p.

1331 Jordá, J.F., 1988. Los travertinos del extremo oriental de la costa de Málaga. Actas del II
1332 Congreso Geológico de España, Universidad de Granada y Sociedad Geológica de España.
1333 Granada, 391-394.

1334 Jordá, J. F., Aura Tortosa, J. E., Álvarez Fernández, E., Avezuela Aristu, B., Badal, E., Maestro
1335 González, A., Villalba Currás, M. P., 2011. Evolución paleogeográfica, paleoclimática y
1336 paleoambiental de la costa meridional de la Península Ibérica durante el Pleistoceno superior. El
1337 caso de la Cueva de Nerja (Málaga, Andalucía, España). Boletín de la Real Sociedad Española
1338 de Historia Natural, 105, 137-147.

1339 Katz, B. G., Griffin, D. W., Davis, J. H., 2009. Groundwater quality impacts from the land
1340 application of treated municipal wastewater in a large karstic spring basin: chemical and
1341 microbiological indicators. Science of the Total Environment, 407, 2872-2886.

1342 Knee, K. L., Street, J. H., Grossman, E. E., Boehm, A. B., Paytan, A., 2010. Nutrient inputs to
1343 the coastal ocean from submarine groundwater discharge in a groundwater-dominated system:
1344 relation to land use (Kona coast, Hawai'i, USA). Limnology and Oceanography, 55, 1105-1122.

1345 Kremer, J. N., Reischauer, A., D’Avanzo, C., 2003. Estuary-specific variation in the air-water
1346 gas exchange coefficient for oxygen. Estuaries and Coasts, 26, 829-836.

1347 Lee, D. R., 1977. A device for measuring seepage flux in lakes and estuaries. Limnology and
1348 Oceanography, 22, 140-147.

1349 Liñán, C., Andreo, B., Carrasco, F., 2000. Caracterización hidrodinámica e hidroquímica del
1350 manantial de Maro (Sierra Almijara, provincia de Málaga). Geogaceta, 27, 95-98.

1351 Macintyre, S., Wannikhof, R., Chanton, J.P., 1995. Trace gas exchange across the air-water
1352 interface in freshwater and coastal marine environments. In: Matson, P.A., Harriss, R.C. (Eds.),
1353 Biogenic Trace Gases: Measuring Emissions from Soil and Water. pp. 52–57.

1354 Martens, C. S., Klump, J. V., Kipphut, G. W., 1980. Sediment-water chemical exchange in the
1355 coastal zone traced by in situ radon-222 flux measurements. Science, 208, 285-288.

1356 Martínez-Santos, P., Andreu, J. M., 2010. Lumped and distributed approaches to model natural
1357 recharge in semiarid karst aquifers. Journal of Hydrology, 388, 389-398.

1358 McCormack, T., Gill, L. W., Naughton, O., Johnston, P. M., 2014. Quantification of
1359 submarine/intertidal groundwater discharge and nutrient loading from a lowland karst catchment.
1360 Journal of Hydrology, 519, 2318-2330.

1361 Mejías, M., García-Orellana, J., Plata, J. L., Marina, M., García-Solsona, E., Ballesteros, B.,
1362 Masqué, P., López, J., Fernández-Arrojo, C., 2008. Methodology of hydrogeological
1363 characterization of deep carbonate aquifers as potential reservoirs of groundwater. Case of study:
1364 the Jurassic aquifer of El Maestrazgo (Castellón, Spain). Environmental Geology, 54, 521-536.

1365 Mejías, M., Ballesteros, B. J., Antón-Pacheco, C., Domínguez, J. A., García-Orellana, J., García-
1366 Solsona, E., Masqué, P., 2012. Methodological study of submarine groundwater discharge from
1367 a karstic aquifer in the Western Mediterranean Sea. Journal of Hydrology, 464, 27-40.

1368 Moore, W. S., 1976. Sampling ^{228}Ra in the deep ocean. Deep Sea Research and Oceanographic
1369 Abstracts, 23, 647-651.

Moore, W. S., 1996. Large groundwater inputs to coastal waters revealed by ^{226}Ra enrichments. Nature, 380, 612-614.

Moore, W. S., Arnold, R., 1996. Measurement of ^{223}Ra and ^{224}Ra in coastal waters using a delayed coincidence counter. Journal of Geophysical Research, 101, 1321-1329.

Moore, W. S., 2000. Determining coastal mixing rates using radium isotopes. Continental Shelf Research, 20, 1993-2007.

Moore, W. S., 2006. Radium isotopes as tracers of submarine groundwater discharge in Sicily. Continental Shelf Research, 26, 852-861.

Moore, W. S., 2008. Fifteen years experience in measuring ^{224}Ra and ^{223}Ra by delayed-coincidence counting. Marine Chemistry, 109, 188-197.

Moore, W. S., 2010. The effect of submarine groundwater discharge on the ocean. Annual Review of Marine Science, 2, 59-88.

Null, K. A., Knee, K. L., Crook, E. D., de Sieyes, N. R., Rebolledo-Vieyra, M., Hernández-Terrones, L., Paytan, A., 2014. Composition and fluxes of submarine groundwater along the Caribbean coast of the Yucatan Peninsula. Continental Shelf Research, 77, 38-50.

Pérez-Ramos, I. Andreo, B., 2007. Masas de aguas subterráneas de Alberquillas y Sierra Almijara. Atlas hidrogeológico de la Provincia Málaga. Coordinador general Duran, J. J. Instituto Geológico y Minero de España, Diputación de Malaga. Tomo 2, 143-148.

Peterson, R. N., Burnett, W. C., Glenn, C. R., Johnson, A. G., 2009. Quantification of point-source groundwater discharges to the ocean from the shoreline of the Big Island, Hawaii. Limnol. Oceanogr, 54, 890-904.

1391 Pinault, J. L., Dörfliger, N., Ladouche, B., Bakalowicz, M., 2004. Characterizing a coastal karst
1392 aquifer using an inverse modeling approach: The saline springs of Thau, southern France. Water
1393 Resources Research, 40, W08501, 1-17.

1394 Pluhowski, E. J., 1972. Hydrologic interpretations based on infrared imagery of Long Island,
1395 New York. USGS Water-Supply paper 2009-B.

1396 Rapaglia, J., Grant, C., Bokuniewicz, H., Pick, T., Scholten, J., 2015. A GIS typology to locate
1397 sites of submarine groundwater discharge. Journal of Environmental Radioactivity, 145, 10-18.

1398 Rapport, D. J., Whitford, W. G., 1999. How Ecosystems Respond to Stress Common properties
1399 of arid and aquatic systems. BioScience, 49, 193-203.

1400 Rodellas, V., García-Orellana, J., García-Solsona, E., Masqué, P., Domínguez, J. A., Ballesteros,
1401 B. J., Mejías, M., Zarroca, M., 2012. Quantifying groundwater discharge from different sources
1402 into a Mediterranean wetland by using ^{222}Rn and Ra isotopes. Journal of Hydrology, 466, 11-22.

1403 Rodellas, V., García-Orellana, J., Tovar-Sánchez, A., Basterretxea, G., López-García, J. M.,
1404 Sánchez-Quiles, D., García-Solsona, E., Masqué, P., 2014. Submarine groundwater discharge as
1405 a source of nutrients and trace metals in a Mediterranean bay (Palma Beach, Balearic Islands).
1406 Marine Chemistry, 160, 56-66.

1407 Rodellas, V., García-Orellana, J., Masqué, P., Feldman, M., Weinstein, Y., 2015. Submarine
1408 groundwater discharge as a major source of nutrients to the Mediterranean Sea. Proceedings of
1409 the National Academy of Sciences, 112, 3926-3930.

1410 Rosenberry, D. O., 2008. A seepage meter designed for use in flowing water. Journal of
1411 Hydrology, 359, 118-130.

1412 Sadat-Noori, M., Santos, I. R., Sanders, C. J., Sanders, L. M., Maher, D. T., 2015. Groundwater
1413 discharge into an estuary using spatially distributed radon time series and radium
1414 isotopes. Journal of Hydrology, 528, 703-719.

1415 Santos, I. R., Burnett, W. C., Chanton, J., Dimova, N., Peterson, R. N. (2009). Land or ocean?:
1416 Assessing the driving forces of submarine groundwater discharge at a coastal site in the Gulf of
1417 Mexico. Journal of Geophysical Research: Oceans, 114, C04012, 1-11.

1418 Schincariol, R. A., McNeil, J. D., 2002. Errors with small volume elastic seepage meter bags.
1419 Ground water, 40, 649-651.

1420 Smith, C. G., Swarzenski, P. W., 2012. An investigation of submarine groundwater—borne
1421 nutrient fluxes to the west Florida shelf and recurrent harmful algal blooms. Limnology and
1422 oceanography, 57, 471-485.

1423 Stamatis, G., Migiros, G., Kontari, A., Dikarou, E., Gamvroula, D., 2011. Application of tracer
1424 method and hydrochemical analyses regarding the investigation of the coastal karstic springs and
1425 the submarine spring (Anavalos) in Stoupa Bay (W. Mani Peninsula). Advances in the Research
1426 of Aquatic Environment Springer Berlin Heidelberg, 459-467.

1427 Stieglitz, T. C., Cook, P. G., Burnett, W. C., 2010. Inferring coastal processes from regional-
1428 scale mapping of 222 Radon and salinity: examples from the Great Barrier Reef, Australia.
1429 Journal of environmental radioactivity, 101, 544-552.

1430 Stringfield, V. T., LeGrand, H. E., 1971. Effects of karst features on circulation of water in
1431 carbonate rocks in coastal areas. Journal of Hydrology, 14, 139-157.

1432 Sun, Y., Torgersen, T., 1998. The effects of water content and Mn-fiber surface conditions on
1433 224Ra measurement by 220Rn emanation. Marine Chemistry, 62, 299-306.

1434 Surić, M., Lončarić, R., Buzjak, N., Schultz, S. T., Šangulin, J., Maldini, K., Tomas, D., 2015.
1435 Influence of submarine groundwater discharge on seawater properties in Rovanjska-Modrič karst
1436 region (Croatia). Environmental Earth Sciences, 74, 5625-5638.

1437 Tamborski, J. J., Rogers, A. D., Bokuniewicz, H. J., Cochran, J. K., Young, C. R., 2015.
1438 Identification and quantification of diffuse fresh submarine groundwater discharge via airborne
1439 thermal infrared remote sensing. Remote Sensing of Environment, 171, 202-217.

1440 Taniguchi, M., Burnett, W. C., Cable, J. E., Turner, J. V., 2002. Investigation of submarine
1441 groundwater discharge. Hydrological Processes, 16, 2115-2129.

1442 Taniguchi, M., Ishitobi, T., Saeki, K. I., 2005. Evaluation of time-space distributions of
1443 submarine ground water discharge. Ground Water, 43, 336-342.

1444 Taniguchi, M., Ishitobi, T., Chen, J., Onodera, S. I., Miyaoka, K., Burnett, W. C., Peterson, R.,
1445 Liu, G., Fukushima, Y., 2008. Submarine groundwater discharge from the Yellow River delta to
1446 the Bohai Sea, China. Journal of Geophysical Research: Oceans, 113, C06025, 1-11.

1447 Theodorou, J. A., James, R., Tzovenis, I., Hellio, C., 2015. The recruitment of the endangered
1448 fan mussel Pinna nobilis (Linnaeus, 1758) on the ropes of a Mediterranean mussel long line
1449 farm. Journal of Shellfish Research, 34, 409-414.

1450 Tomas, J., Aznar, F. J., Raga, J. A., 2001. Feeding ecology of the loggerhead turtle Caretta
1451 caretta in the western Mediterranean. Journal of Zoology, 255, 525-532.

1452 Tovar-Sánchez, A., Basterretxea, G., Rodellas, V., Sánchez-Quiles, D., García-Orellana, J.,
1453 Masqué, P., García-Solsona, E., 2014. Contribution of groundwater discharge to the coastal
1454 dissolved nutrients and trace metal concentrations in Majorca Island: karstic vs detrital systems.
1455 Environmental Science Technology, 48, 11819-11827.

1456 Trezzi, G., García-Orellana, J., Rodellas, V., Santos-Echeandia, J., Tovar-Sánchez, A., García-
1457 Solsona, E., Masqué, P., 2016. Submarine groundwater discharge: A significant source of
1458 dissolved trace metals to the North Western Mediterranean Sea. Marine Chemistry, 186, 90-100.

1459 Trezzi, G., García-Orellana, J., Rodellas, V., Masqué, P., García-Solsona, E., Andersson, P. S.,
1460 2017. Assessing the role of submarine groundwater discharge as a source of Sr to the
1461 Mediterranean Sea. Geochimica et Cosmochimica Acta, 200, 42-54.

1462 Valiela, I., Foreman, K., LaMontagne, M., Hersh, D., Costa, J., Peckol, P., DeMeo-Andreson, B.,
1463 D'Avanzo, C., Babione, M., Sham, C.H., Brawley, J., 1992. Couplings of watersheds and coastal
1464 waters: sources and consequences of nutrient enrichment in Waquoit Bay, Massachusetts.
1465 Estuaries, 15, 443-457.

1466 Valiela, I., Cole, M. L., 2002. Comparative evidence that salt marshes and mangroves may
1467 protect seagrass meadows from land-derived nitrogen loads. Ecosystems, 5, 92-102.

1468 Webster, I. T., Hancock, G. J., Murray, A. S., 1995. Modelling the effect of salinity on radium
1469 desorption from sediments. Geochimica et Cosmochimica Acta, 59, 2469-2476.

1470 Weinstein, Y., Yechieli, Y., Shalem, Y., Burnett, W. C., Swarzenski, P. W., Herut, B., 2011.
1471 What is the role of fresh groundwater and recirculated seawater in conveying nutrients to the
1472 coastal ocean? Environmental Science Technology, 45, 5195-5200.

Wong, W. W., Grace, M. R., Cartwright, I., Cardenas, M. B., Zamora, P. B., Cook, P. L., 2013. Dynamics of groundwater-derived nitrate and nitrous oxide in a tidal estuary from radon mass balance modeling. Limnol. Oceanogr, 58, 1689-1706.

Worthington, S. R. H., 1999. A comprehensive strategy for understanding flow in carbonate aquifers. In Palmer A. N., Palmer M. V., Sasowsky I. D. (Eds), Karst Modeling. Karst Waters Institute, pp. 30-37.

Yobbi, D. K., 1992. Effects of tidal stage and ground-water levels on the discharge and water quality of springs in coastal Citrus and Hernando Counties, Florida, US Department of the Interior. US Geological Survey, 44 p.

List of Tables

Table 1: Summary of values for all terms used to solve the radium and salinity mass balances to asses submarine springs discharge in the karst section. Calculated total flux (F_{SGD}) using both methods are also shown.

Table 2: Parameters used in the radon mass balance to asses diffuse seepage in Maro Cliff (conglomerate section) and Cantarrijan Beach (karst section) including estimated groundwater fluxes (F_{SGD}).

Table 3: Comparison of groundwater seepage velocities estimated via radon model and seepage meters during July of 2016 (dry period) in Maro Cliff (conglomerate section) and Cantarrijan Beach (karst section).

Table 4: Summary of total groundwater discharge (TGD) including all modes of discharge (CS, GC, GS, SS), and fresh groundwater discharge from the Sierra Almijara-Alberquillas (SAA) aquifer (daily and annual). Total nitrate fluxes to coastal waters (N-TGD) in the three sections (conglomerate, Schist, and Karst sections), with respect to agricultural coverage. Relative agricultural area represents the coverage normalized by the total extension of each section near the coast.

Table 5: Values of all parameters applied in the sensitivity analysis including flux ranges estimated for each methodology.

Table 6: Applicability comparison of all methods utilized to detect and quantify different modes of groundwater discharge to the sea. Flux ranges are based on maxima and minima estimations obtained in

1521 the sensitivity analysis. Daily fluxes are shown for each form of discharge and method, and annual water
1522 budget (fresh) of Sierra Almijara-Alberquillas (SAA).

	Radium (1) mass balance			Salinity mass balance (2)					
	Ra_{sw}	Ra_{SGD}	Ra_{ow}	Sal_{sw}	Sal_{SGD}	Sal_{ow}	V	F_{SGD} (1)	F_{SGD} (2)
		(dpm m^{-3})					($\times 10^5$ m^3)	($\times 10^3$ m^3 d^{-1})	
Cantarrijan	25 ± 2	1260 ± 90	8 ± 1	36.3 ± 0.1	0.0	36.5	2.67	4.7 ± 0.5	0.8 ± 0.1
Palomas	18 ± 2	1260 ± 90	8 ± 1	36.4 ± 0.1	0.0	36.5	4.04	4.3 ± 0.5	0.9 ± 0.1
Sifon	17 ± 2	1260 ± 90	8 ± 1	36.4 ± 0.1	0.0	36.5	3.72	3.7 ± 0.4	0.5 ± 0.1
Total flux								12.8 ± 1.4	2.3 ± 0.2

Table 1

		Rn_{SGD}	$F_{Waterfall}$	C_{Ra}	F_{Diff}	F_{Mix}	F_{Atm}	Seepage Area	SGD	F_{SGD}
		($\times 10^3$ dpm m^{-3})	($\times 10^3$ dpm m^{-2} d^{-1})	(dpm m^{-3})	(dpm m^{-2} d^{-1})	($\times 10^3$ dpm m^{-2} d^{-1})		($\times 10^3$ m^2)	(cm d^{-1})	($\times 10^3$ m^3 d^{-1})
Maro Cliff	Jul-15	350 ± 50	16 ± 6	280 ± 50	619 ± 57	149 ± 40	33 ± 9	7.7	39 ± 10	3.0 ± 0.8
	Dec-15	440 ± 60	21 ± 8	280 ± 50	619 ± 57	238 ± 64	11 ± 3	7.7	40 ± 11	3.1 ± 0.8
	Jul-16	320 ± 30	10 ± 5	280 ± 50	619 ± 57	160 ± 43	25 ± 7	7.7	38 ± 10	2.9 ± 0.7
Cantarrijan Beach	Jul-15	310 ± 70	N/A	170 ± 40	455 ± 51	-		4.3	-	-
	Dec-15	240 ± 60	N/A	170 ± 40	455 ± 51	84 ± 13	30 ± 5	4.3	52 ± 8	2.3 ± 0.3
	Jul-16	350 ± 40	N/A	170 ± 40	455 ± 51	115 ± 18	27 ± 4	4.3	22 ± 3	0.9 ± 0.1

Table 2

	SGD seepage rate (cm d^{-1})	
	Maro Cliff	Cantarrijan Beach
Radon model	38 ± 10	22 ± 3
Seepage meters	28 ± 7	23 ± 7
SM-1	19	13
SM-2	32	32
SM-3	37	26
SM-4	25	20
SM-5		0
SM-6		1
SM-7		0
SM-8		0
SM-9		1

Table 3

	TGD	CS	GC	GS	SS	Fresh TGD from SAA	Annual budget SAA	Agricultural area	Relative agricultural area	N-TGD
	($\times 10^3$ m^3 d^{-1})		($\times 10^3$ m^3 d^{-1})			($\times 10^3$ m^3 d^{-1})	($\times 10^6$ m^3 y^{-1})	(km^2)	(%)	(mol d^{-1})
Conglomerate section	3.5 – 4.0	0.5 – 0.8	0.1 – 0.2	2.9 – 3.0	0	0.1 – 0.2	0.06 – 0.08	204	95	550 - 732
Schist section	2.4 – 3.6	1.1 – 1.6	1.3 – 2.0	0	0	2.3 – 3.4	0.8 – 1.2	103	7	136 – 204
Karst section	3.0 – 4.8	0	0	0.9 – 2.3	2.1 – 2.5	2.5 – 3.6	1.0 – 1.3	0	0	18 – 53

Table 4

Method/Form of discharge	Model parameters										Final SGD estimate (x 10 m^3 d^{-1})	Percentage difference between min and max estimate
	Residence time (days)	^{224}Ra gw end-member (dpm m^{-3})	Salinity isoline	Volume SGD plume (x 10^5 m^3)			^{222}Rn isoline (x 10^3 dpm m^{-3})		Seepage area (x 10^3 m^2)			
				Cantarrijan	Palomas	Sifon	Maro Cliff	Cantarrijan Beach	Maro Cliff	Cantarrijan Beach		
Salinity mass balance/Submarine springs	0.25	N/A	-0.3	0.9	1.5	1.1	N/A	N/A	N/A	N/A	0.2 - 90.5	100%
	0.50	N/A	0.0	2.6	4.0	3.7	N/A	N/A	N/A	N/A		
	1.00	N/A	0.3	2.8	5.4	4.7	N/A	N/A	N/A	N/A		
	3.00	N/A	0.6	4.6	8.7	7.1	N/A	N/A	N/A	N/A		
	0.5 m water column		0.0	0.20	0.18	0.19	N/A	N/A	N/A	N/A		
^{224}Ra mass balance/Submarine springs	0.25	1020 ± 80	-0.3	0.9	1.5	1.1	N/A	N/A	N/A	N/A	0.03 - 13.5	100%
	0.50		0.0	2.6	4.0	3.7	N/A	N/A	N/A	N/A		
	1.00	1260 ± 90	0.3	2.8	5.4	4.7	N/A	N/A	N/A	N/A		
	3.00		0.6	4.6	8.7	7.1	N/A	N/A	N/A	N/A		
	0.5 m water column		0.0	0.20	0.18	0.19	N/A	N/A	N/A	N/A		
^{222}Rn mass balance/Diffuse seepage	N/A	N/A	N/A	N/A	N/A	N/A	25	5	2.4	1.0	1.1 - 10.0	89%
	N/A	N/A	N/A	N/A	N/A	N/A	30	6	7.7	3.2		
	N/A	N/A	N/A	N/A	N/A	N/A	35	8	10.6	4.3		
	N/A	N/A	N/A	N/A	N/A	N/A	45	10	17.8	5.7		
Seepage meters/Diffuse seepage	N/A	N/A	N/A	N/A	N/A	N/A	25	5	2.4	1.0	1.2 - 9.1	87%
	N/A	N/A	N/A	N/A	N/A	N/A	30	6	7.7	3.2		
	N/A	N/A	N/A	N/A	N/A	N/A	35	8	10.6	4.3		
	N/A	N/A	N/A	N/A	N/A	N/A	45	10	17.8	5.7		

Table 5

Mode of groundwater (GW) discharge / site name	^{224}Ra method		^{222}Rn method		Salinity method		Seepage meter method		Flow meter method
	Obs. anomaly in seawater	Flux ($\times 10^3$ m^3 d^{-1})	Obs. anomaly in seawater	Flux ($\times 10^3$ m^3 d^{-1})	Obs. anomaly in seawater	Flux ($\times 10^3$ m^3 d^{-1})	Obs. anomaly in seawater	Flux ($\times 10^3$ m^3 d^{-1})	Flux ($\times 10^3$ m^3 d^{-1})
GW-fed creeks Caleta Tierras Nuevas Miel	✓	N/A	×	N/A	✓	N/A	×	N/A	1.4 – 2.2
Coastal springs Doncellas Barranco Maro Huerto Romero Maro Beach Alberquillas	×	N/A	×	N/A	✓	N/A	×	N/A	1.6 – 2.4
Submarine springs Cantarrijan Palomas Sifon	✓	0.2 – 90.5	×	N/A	✓	0.03 – 13.5	×	N/A	N/A
Diffused seepage Maro Cliff Cantarrijan Beach	×	N/A	✓	1.1 – 10.0	✓	N/A	✓	1.2 – 9.1	N/A

Table 6

List of figures

Figure 1: Study site location and geological map showing water table contour lines (from Pérez-Ramos and Andreo, 2007), groundwater flow direction, important wells and piezometers, sampling points, and terrestrial springs. Groundwater discharge to the sea (TGD) is represented in purple and is based on this study. Coastal springs are represented as CS, groundwater-fed creeks as GC, diffuse groundwater seepage as GS, and submarine springs as SS. The study area is divided in three sections: conglomerate section, schist section, and karst section. The distribution of seagrass beds are based on Bañares-España et al. (2002), and Aranda and Otero (2014).

Figure 2: Average monthly precipitation and sea level change during 2010, 215, and 2016. Error bars show the monthly rainfall variability during this study. In December of 2015 slight precipitation occurred only during the first week, however, abundant rainfall took place during September-November. Sea level showed minima values during January-May and maxima during August-December. Sampling campaigns were conducted during May-July (dry periods) and December (wet periods).

Figure 3: Interpolated ^{224}Ra activity concentrations in September of 2010 along the schist and karst sections. Two areas of high ^{224}Ra in coastal waters were identified in the schist section near groundwater-fed Miel Creek (56 ± 4 dpm m^{-3}), and the three clustered submarine springs discharging from Cantarrijan Caves (51 ± 4 dpm m^{-3}) located in the Cantarrijan area (karst section).

Figure 4: Salinity anomaly map showing combined results from May, July, and December of 2015. Two areas of negative salinity anomalies were found in the conglomerate (salinity anomaly = -1.2 to -1.7) and karst (salinity anomaly = -0.3 to -1.0) sections almost perfectly aligned with their delineated extent.

Figure 5: Radon-222 distribution map based on surveys during July and December of 2015, and July of 2016. Two radon peaks were in found in Maro Cliff (conglomerate section) and Cantarrijan Beach (karst section) with maximum concentrations of $44 \pm 3 \times 10^3$ dpm m^{-3} and $30 \pm 2 \times 10^3$ dpm m^{-3} respectively.

Figure 6: (a) Groundwater seepage velocity averaging results from radon mass balance and seepage meters in areas of diffuse seepage (Maro Cliff and Cantarrijan Beach). Radon distribution in (b) Maro Cliff (conglomerate section) and (c) Cantarrijan Beach (karst section) where cylinder symbols represent seepage meter locations and the star radon time series stations.

Figure 7: Radon fluxes result of each component of the mass balance box model during all sampling campaigns in Maro Cliff (conglomerate section) and Cantarrijan Beach (karst section). The largest tracer losses occurred via mixing due to the high exposure of both areas to waves and currents. Greater difference in SGD-^{222}Rn fluxes was found between wet periods (December) and dry periods (July) in Cantarrijan Beach compared to Maro Cliff.

Figure 8: (a) Isotopic composition ($\delta^{18}O$, $\delta^{2}H$) of water samples collected during all sampling campaigns. Local Groundwater Line (LGL) represents the linear trend based on all groundwater

samples collected in the study area. Global Meteoric Water Line (GMWL) is based on Craig, (1961) and the Western Mediterranean Meteoric Water Line (WMMWL) on Gat and Garmi, (1970). White color represents points of discharge in conglomerate and breccia lithology, while light grey are in travertine (conglomerate section); dark grey shows points in schist (schist section); and black color show locations in karstic marble (karst section). Maro Spring and Nerja Cave well (not points of discharge to the sea) are represented with a black and white star respectively. Water samples collected at each section (conglomerate section, schist section, ans karst section) are grouped in dashed squares. (b) Isotopic composition of samples collected from points of discharge from the travertine formation in the conglomerate section. The two groundwater end-members (Maro Spring and irrigation waters) are circled, while diffuse seepage in Maro Cliff is represented with squares.

Figure 9: Mixing plots of ^{224}Ra (a) and ^{222}Rn versus salinity (b) showing best fit linear and exponential mixing lines, respectively, during surface water surveys along the coastline in September of 2010, July and December of 2015.

Figure 10: Total groundwater discharge (TGD) in the study area divided in forms of discharge (GS: groundwater diffuse seepage, CS: coastal springs, GC: groundwater-fed creeks, SS: submarine springs), showing maximum and minimum flux during wet and dry periods.

Figure 11: Groundwater ionic relationship between NO_3^- and SO_4^{2-} where groundwater samples with similar composition are grouped in dashed squares. Symbols are presented as in Fig. 8 based on the section and lithology they are located. In the conglomerate section Maro Spring,

Nerja Cave, and Maro Creek show similar SO_4^{2-} concentration with low NO_3^-, while Doncellas, Barranco Maro, Huerto Romero, and Maro Beach present NO_3^- contamination. Samples from the schist section (Miel and Alberquillas) present a distinctive signal with low NO_3^- and SO_4^{2-} concentrations. Groundwater collected in Cantarrijan Beach (karst section) shows seawater influence from saltwater recirculation in beach sediments. Arrows indicate the geochemical change before irrigation and after fertilizers application (NO_3^-), where Maro cliff (diffuse seepage) shows mixing between both groups.

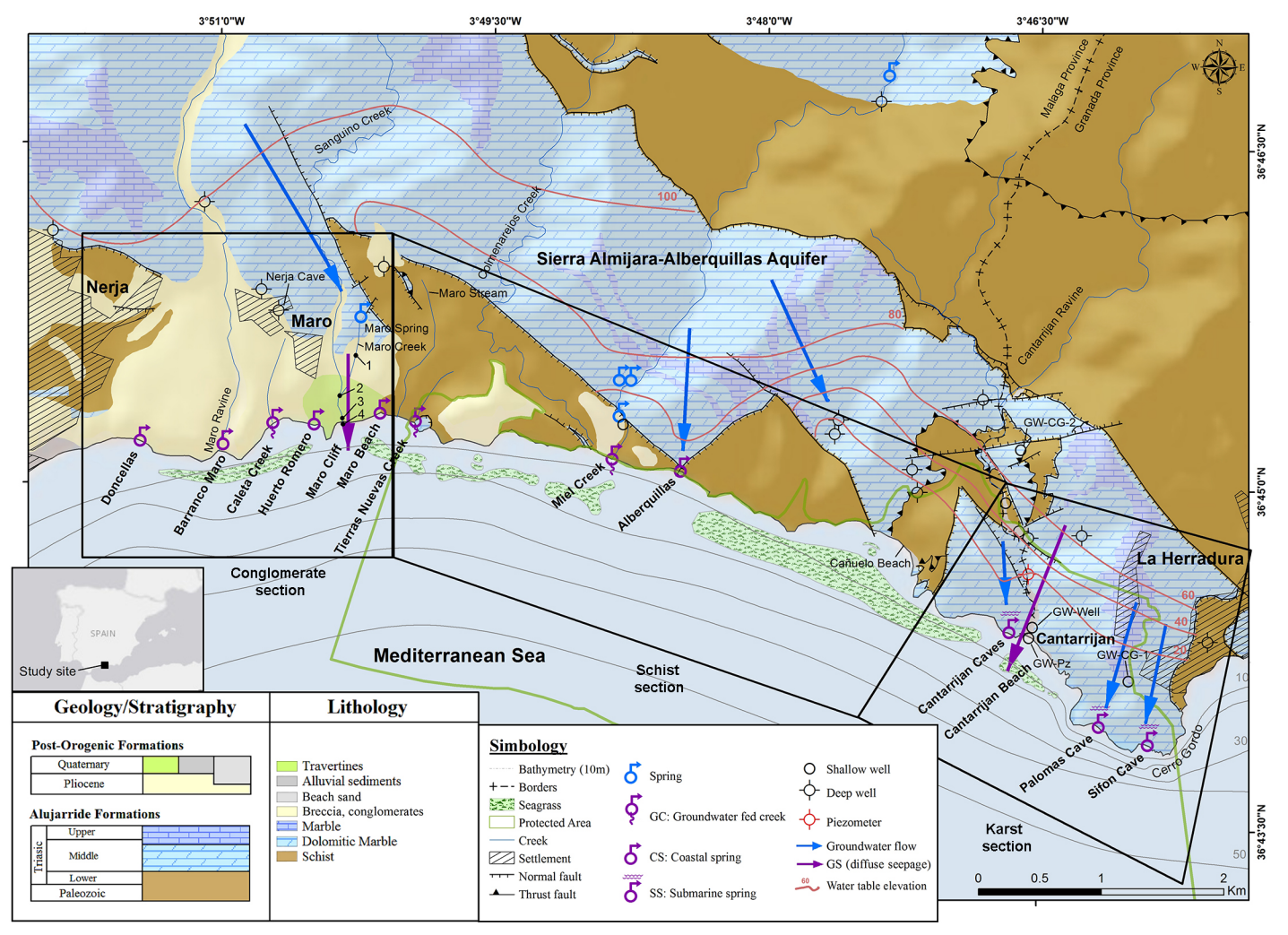

Geology/Stratigraphy

Post-Orogenic Formations

- Quaternary
- Pliocene

Alujarride Formations

- Triasic
  - Upper
  - Middle
  - Lower
- Paleozoic

Lithology

- Travertines
- Alluvial sediments
- Beach sand
- Breccia, conglomerates
- Marble
- Dolomitic Marble
- Schist

Simbology

- Bathymetry (10m)
- Borders
- Seagrass
- Protected Area
- Creek
- Settlement
- Normal fault
- Thrust fault
- Spring
- GC: Groundwater fed creek
- CS: Coastal spring
- SS: Submarine spring
- Shallow well
- Deep well
- Piezometer
- Groundwater flow
- GS (diffuse seepage)
- Water table elevation

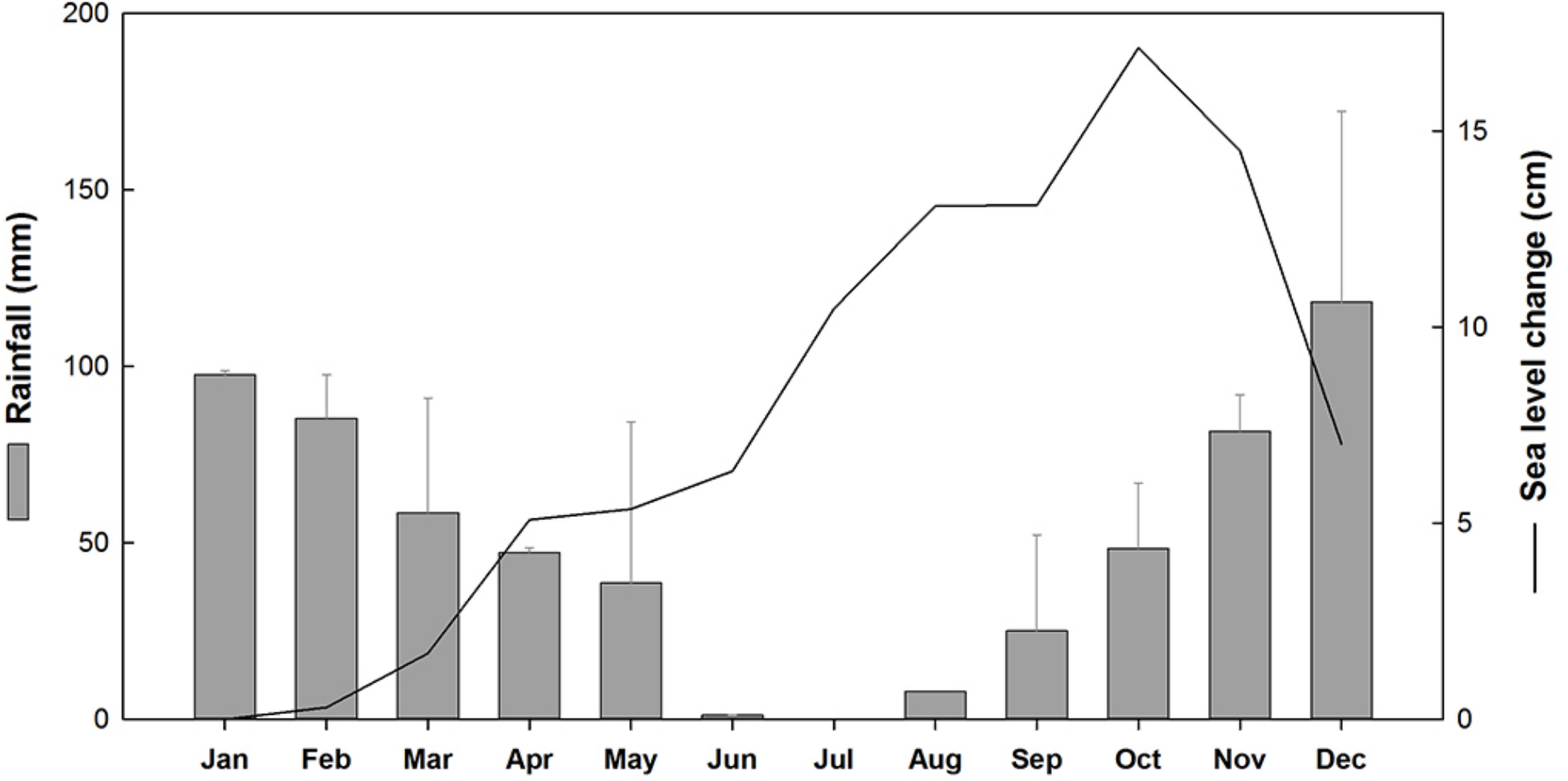
Rainfall (mm)
Sea level change (cm)
200
150
100
50
0
15
10
5
0
Jan
Feb
Mar
Apr
May
Jun
Jul
Aug
Sep
Oct
Nov
Dec

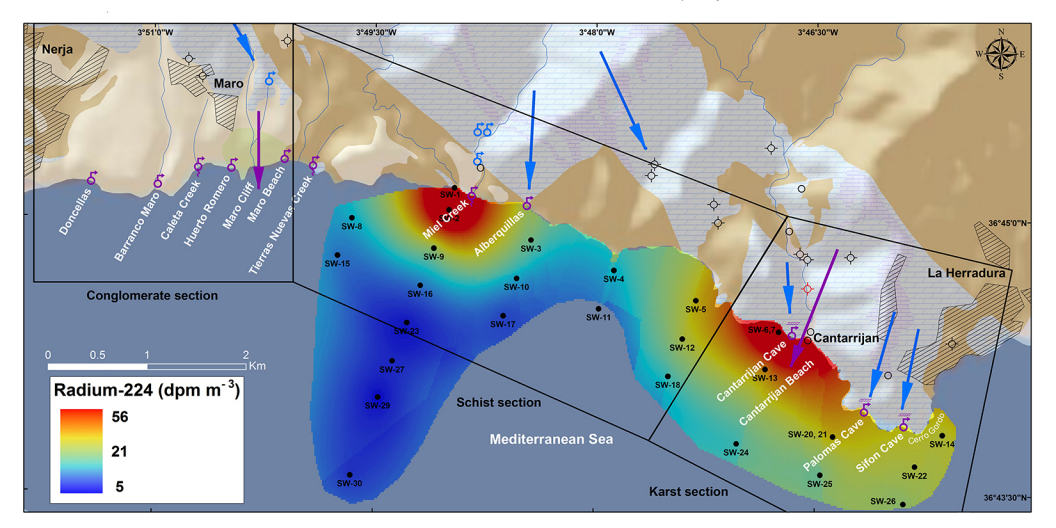
3°51'0"W
3°49'30"W
3°48'0"W
3°46'30"W
36°45'0"N
36°43'30"N
N
W
E
S
Nerja
Maro
Doncellas
Barranco Maro
Caleta Creek
Huerto Romero
Maro Cliff
Maro Beach
Tierras Nuevas Creek
Conglomerate section
Miel Creek
Albercutillas
SW-1
SW-8
SW-9
SW-3
SW-15
SW-16
SW-10
SW-4
SW-23
SW-17
SW-11
SW-27
SW-29
SW-30
Schist section
Mediterranean Sea
Karst section
La Herradura
Cantarrijan
SW-6,7
SW-12
SW-5
SW-13
SW-18
Cantarrijan Cave
Cantarrijan Beach
SW-20, 21
Paloma Cave
Sifon Cave
Cerro Gordo
SW-14
SW-24
SW-22
SW-25
SW-26
0
0.5
1
2
Km
Radium-224 (dpm m-3)
56
21
5

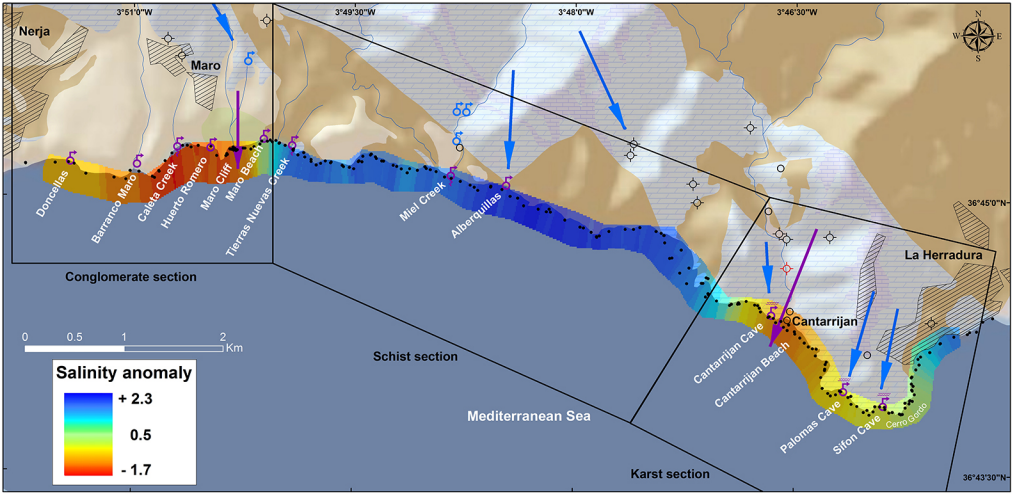
3°51'0"W
3°49'30"W
3°48'0"W
3°46'30"W
36°45'0"N
36°43'30"N
N
W
E
S
Nerja
Maro
La Herradura
Cantarrijan
Conglomerate section
Schist section
Karst section
Mediterranean Sea
Doncellas
Barranco Maro
Calleta Creek
Huerto Romero
Maro Cliff
Maro Beach
Torres Nuevas Creek
Miel Creek
Alberquillas
Cantarrijan Cave
Cantarrijan Beach
Palomas Cave
Sifon Cave
Cerro Gordo
0
0.5
1
2
Km
Salinity anomaly
+ 2.3
0.5
- 1.7

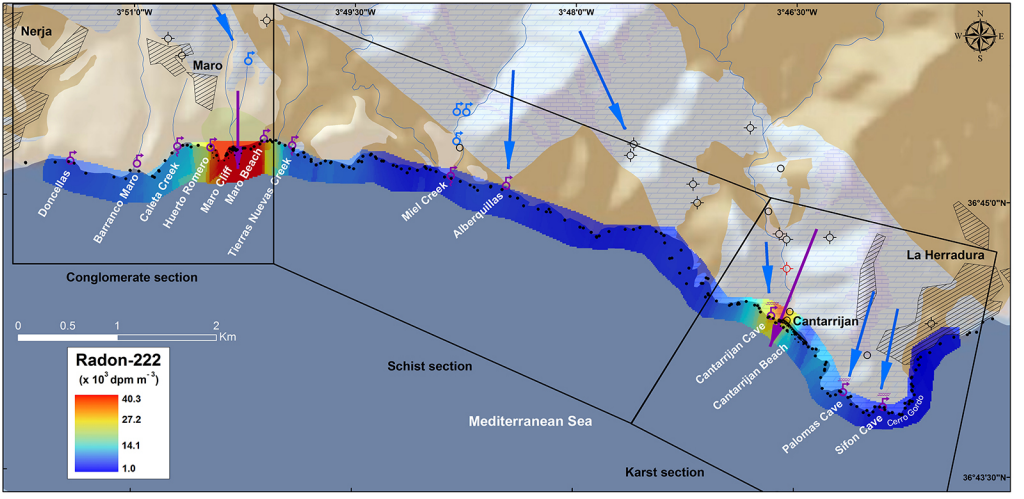
3°51'0"W
3°49'30"W
3°48'0"W
3°46'30"W
36°45'0"N
36°43'30"N
N
W
E
S
Nerja
Maro
Doncellas
Barranco Maro
Calata Creek
Huerto Romero
Maro Cliff
Maro Beach
Tierras Nuevas Creek
Mlei Creek
Alberquillas
La Herradura
Cantarrijan
Cantarrijan Cave
Cantarrijan Beach
Palomas Cave
Sifon Cave
Cerro Gordo
Conglomerate section
Schist section
Karst section
Mediterranean Sea
0
0.5
1
2
Km
Radon-222
(x 10³ dpm m⁻³)
40.3
27.2
14.1
1.0

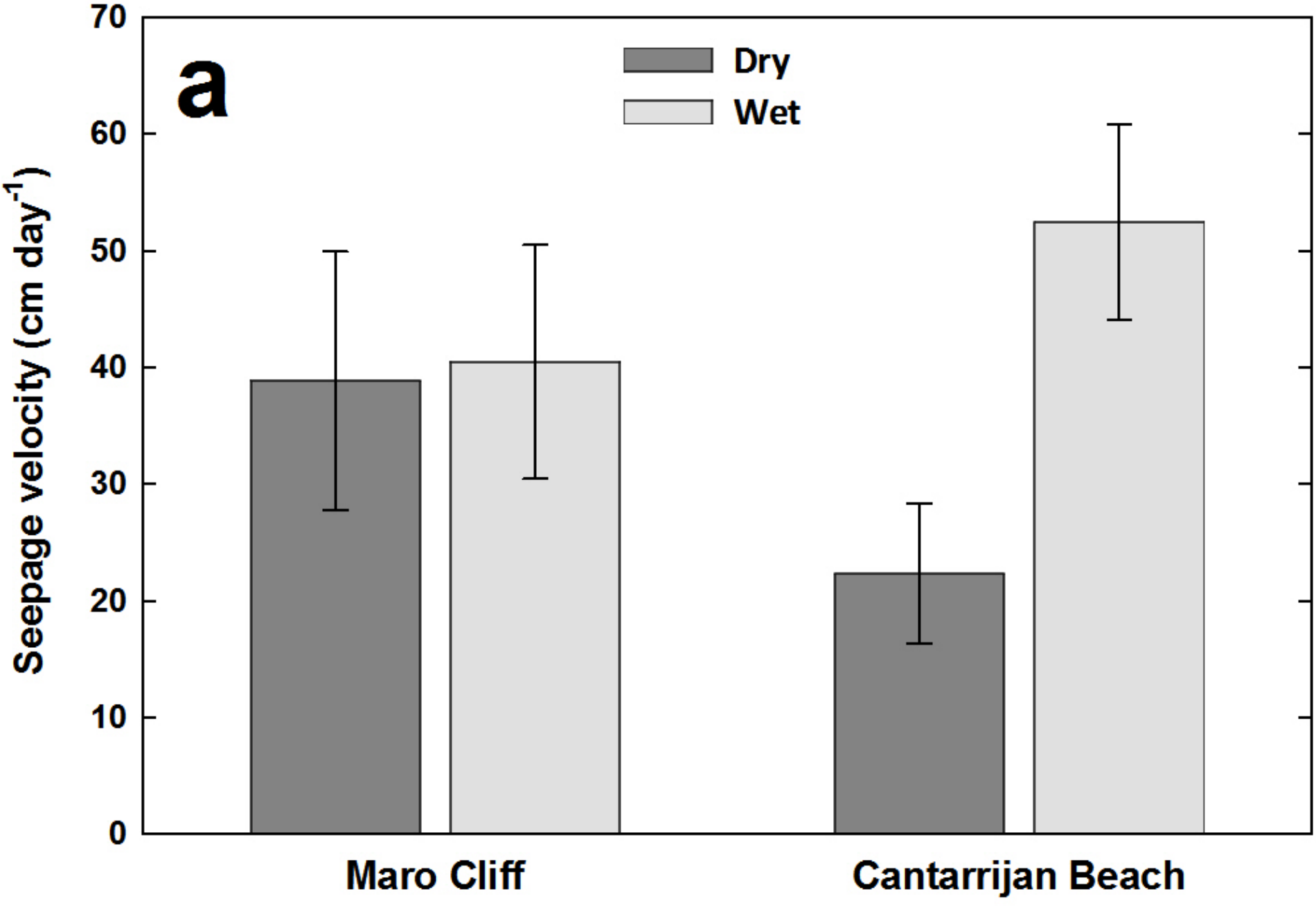
a
Dry
Wet
Seepage velocity (cm day-1)
70
60
50
40
30
20
10
0
Maro Cliff
Cantarrijan Beach

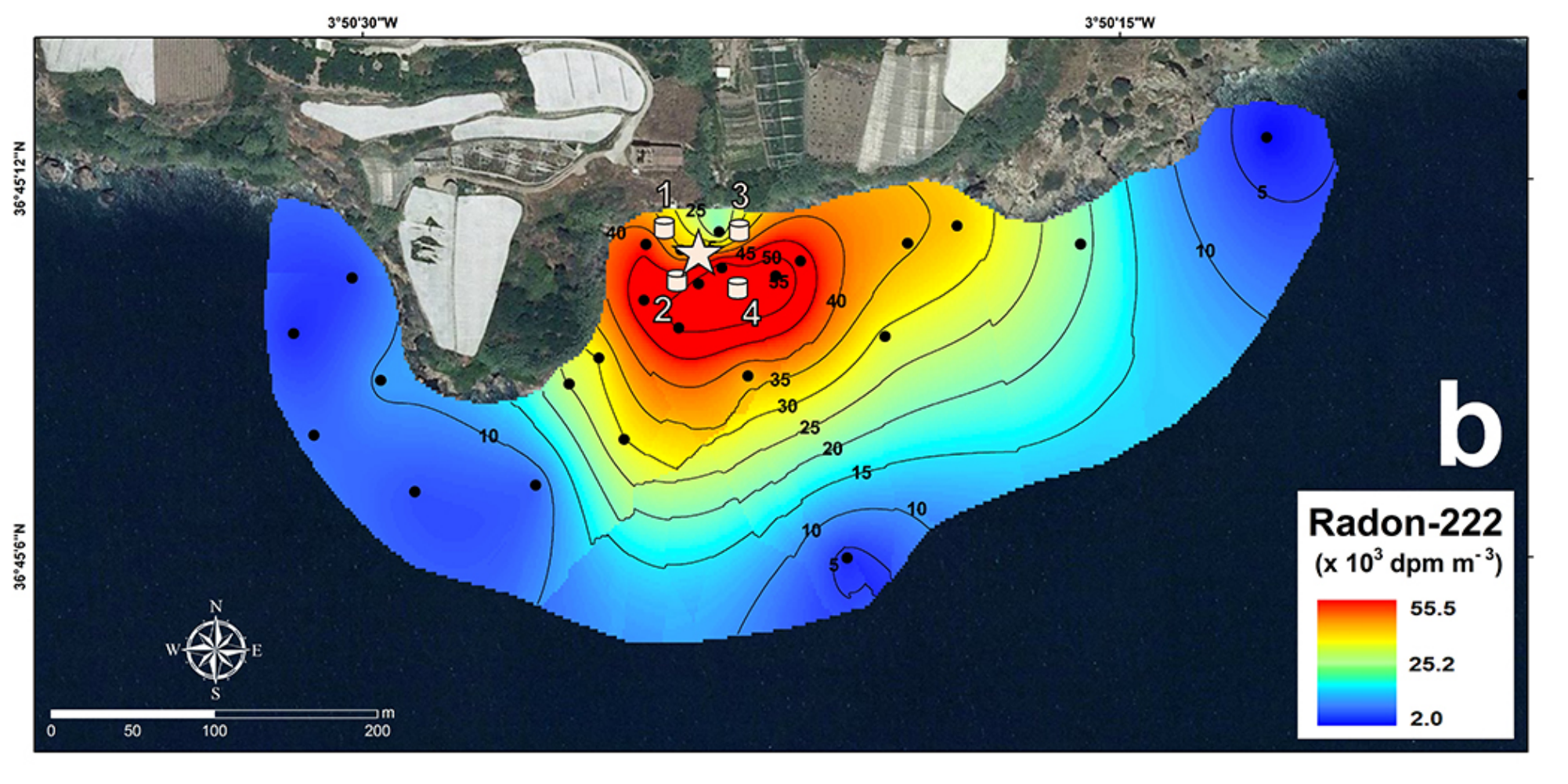
3°50'30"W
3°50'15"W
36°45'12"N
36°45'6"N
1
2
3
4
5
10
15
20
25
30
35
40
45
50
55
b
Radon-222
(x 10³ dpm m⁻³)
55.5
25.2
2.0
N
W
E
S
0
50
100
200
m

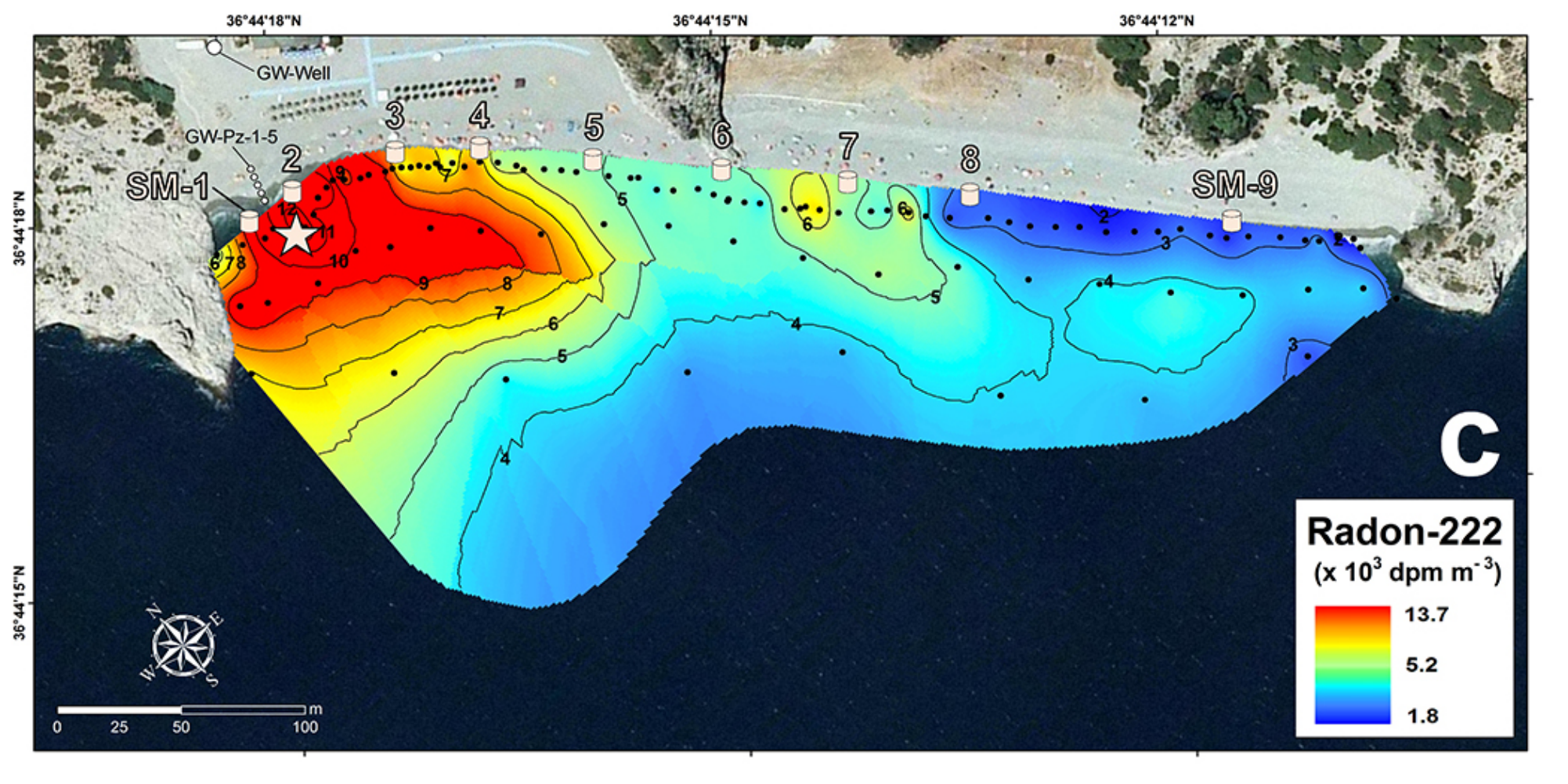
36°44'18"N
36°44'15"N
36°44'12"W
GW-Well
GW-Pz-1-5
SM-1
SM-9
2
3
4
5
6
7
8
C
Radon-222
(x 10³ dpm m⁻³)
13.7
5.2
1.8
N
E
S
W
0
25
50
100
m

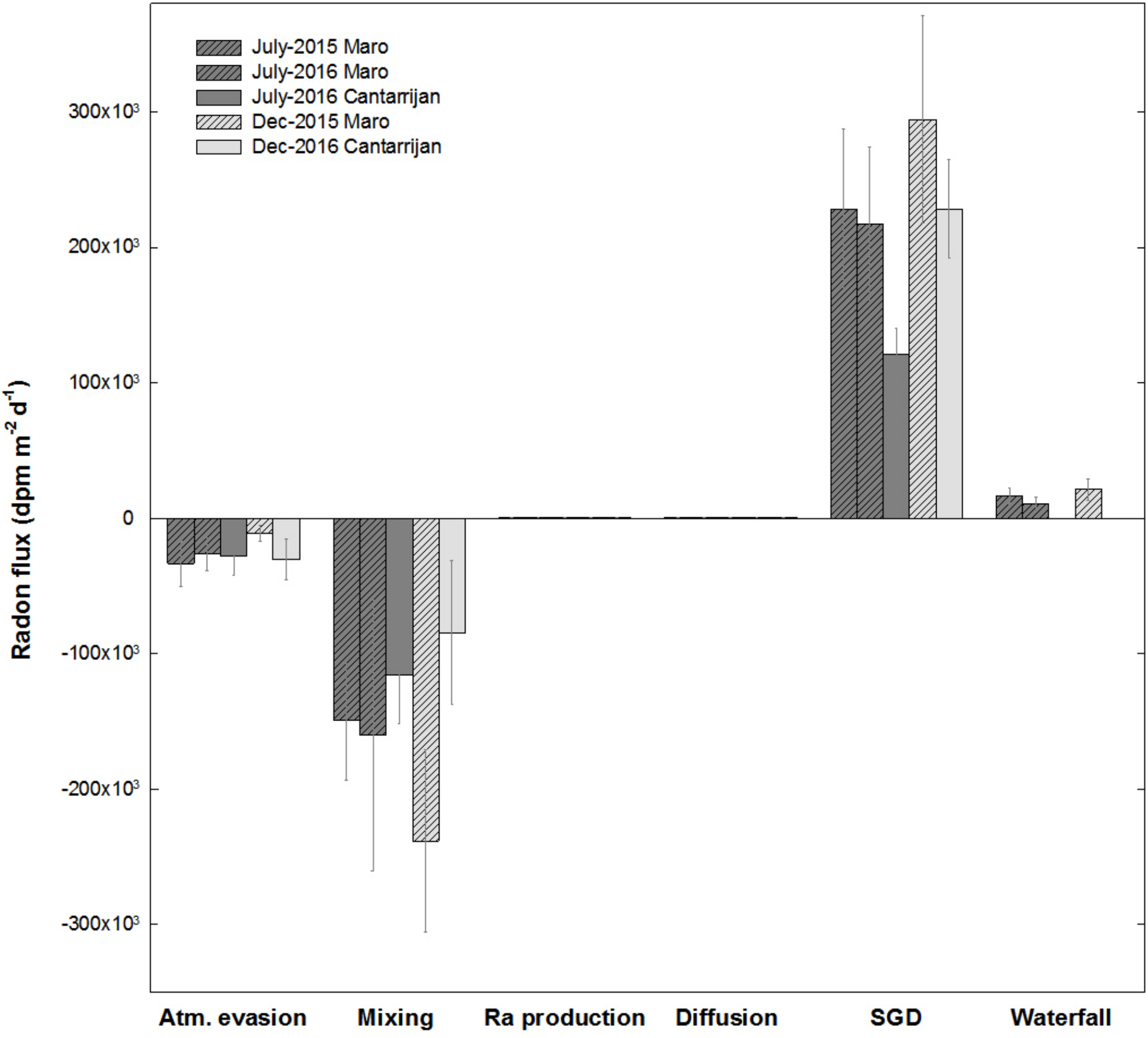
July-2015 Maro
July-2016 Maro
July-2016 Cantarrijan
Dec-2015 Maro
Dec-2016 Cantarrijan
300x10³
200x10³
100x10³
0
-100x10³
-200x10³
-300x10³
Radon flux (dpm m⁻² d⁻¹)
Atm. evasion
Mixing
Ra production
Diffusion
SGD
Waterfall

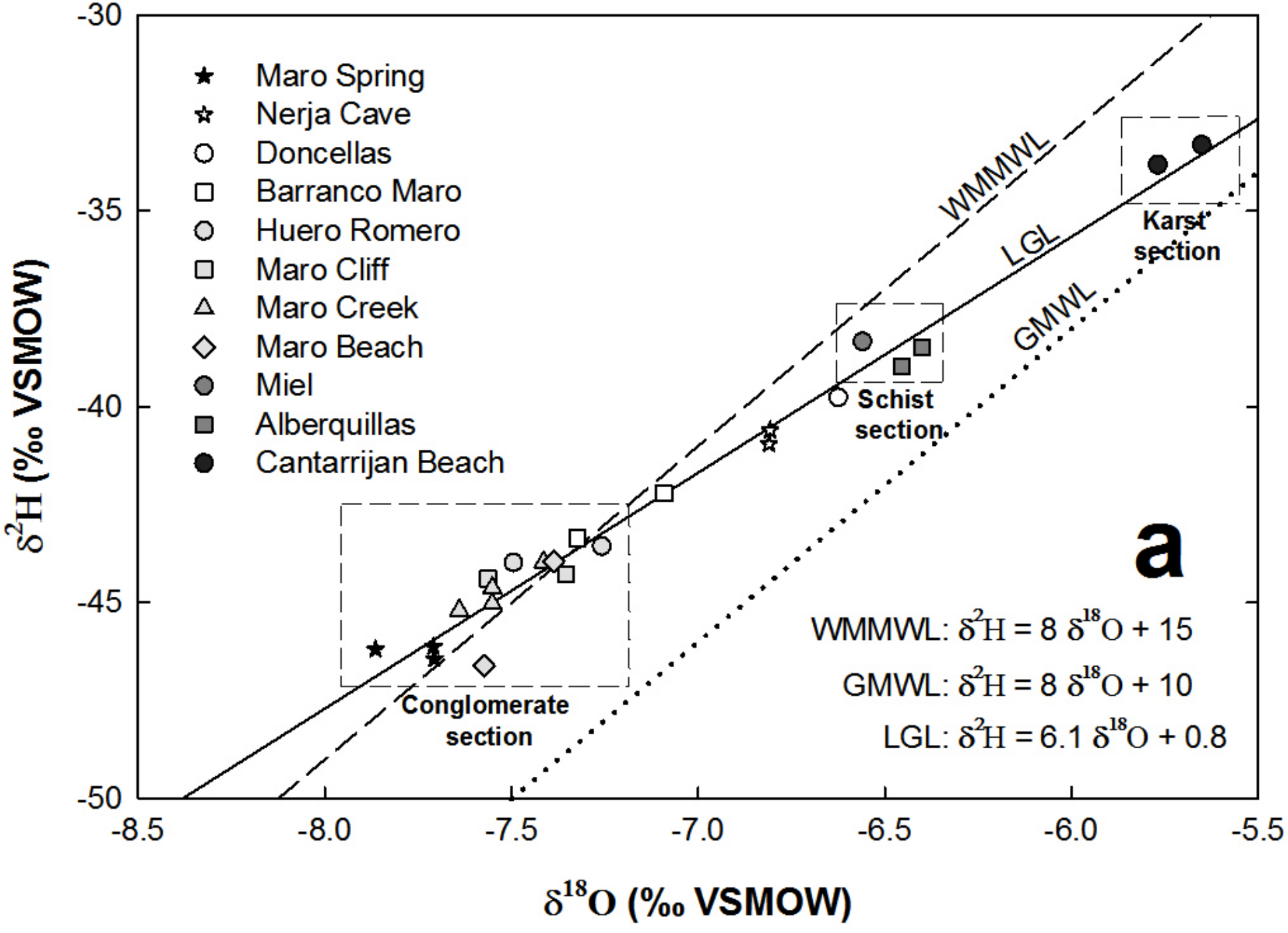
-30
-35
-40
-45
-50
-8.5
-8.0
-7.5
-7.0
-6.5
-6.0
-5.5
δ2H (‰ VSMOW)
δ18O (‰ VSMOW)
Maro Spring
Nerja Cave
Doncellas
Barranco Maro
Huero Romero
Maro Cliff
Maro Creek
Maro Beach
Miel
Alberquillas
Cantarrijan Beach
WMMWL
LGL
GMWL
Karst section
Schist section
Conglomerate section
a
WMMWL: δ2H = 8 δ18O + 15
GMWL: δ2H = 8 δ18O + 10
LGL: δ2H = 6.1 δ18O + 0.8

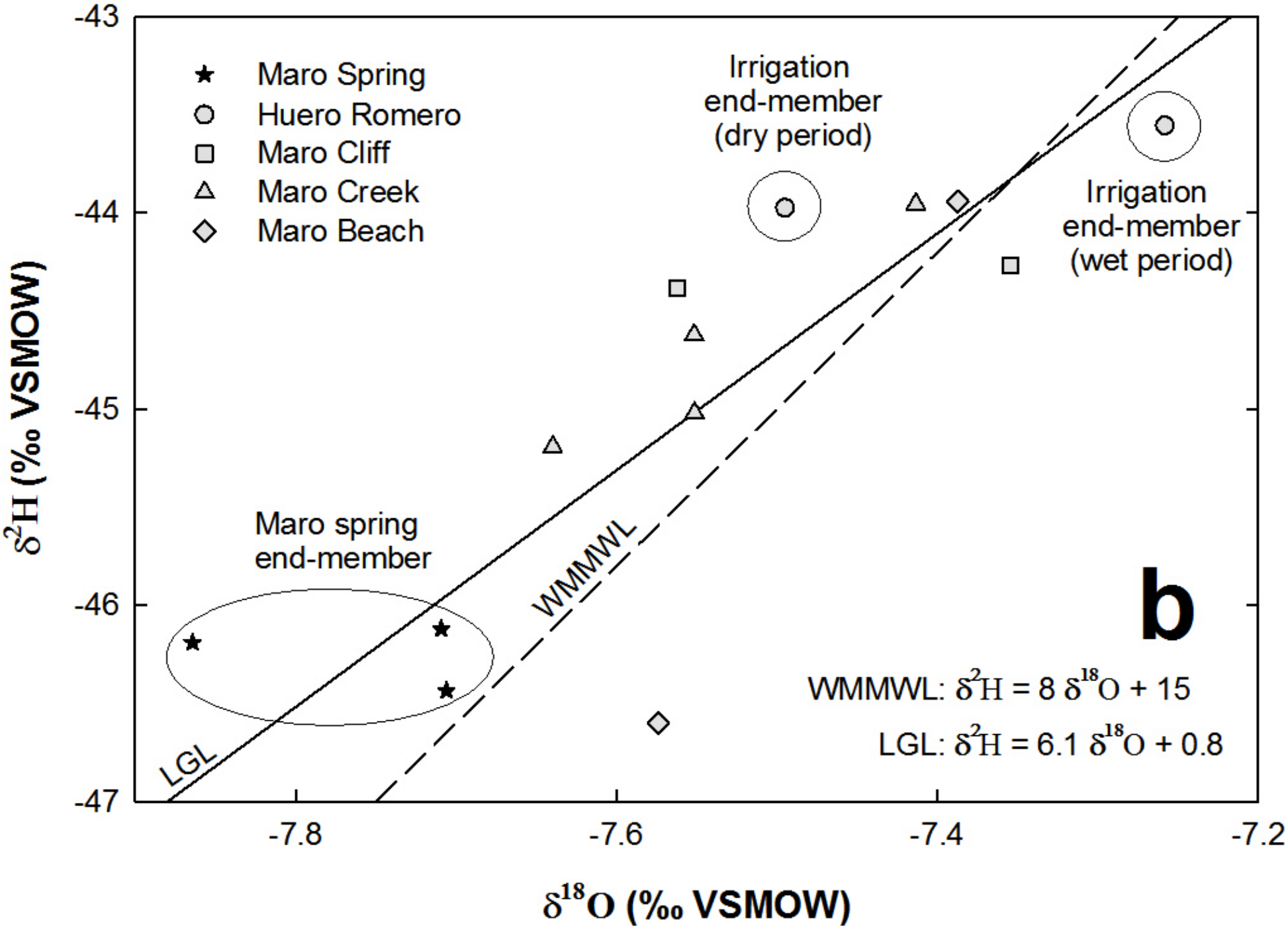
-43
-44
-45
-46
-47
-7.8
-7.6
-7.4
-7.2
δ²H (‰ VSMOW)
δ¹⁸O (‰ VSMOW)
Maro Spring
Huero Romero
Maro Cliff
Maro Creek
Maro Beach
Irrigation end-member (dry period)
Irrigation end-member (wet period)
Maro spring end-member
WMMWL
LGL
b
WMMWL: δ²H = 8 δ¹⁸O + 15
LGL: δ²H = 6.1 δ¹⁸O + 0.8

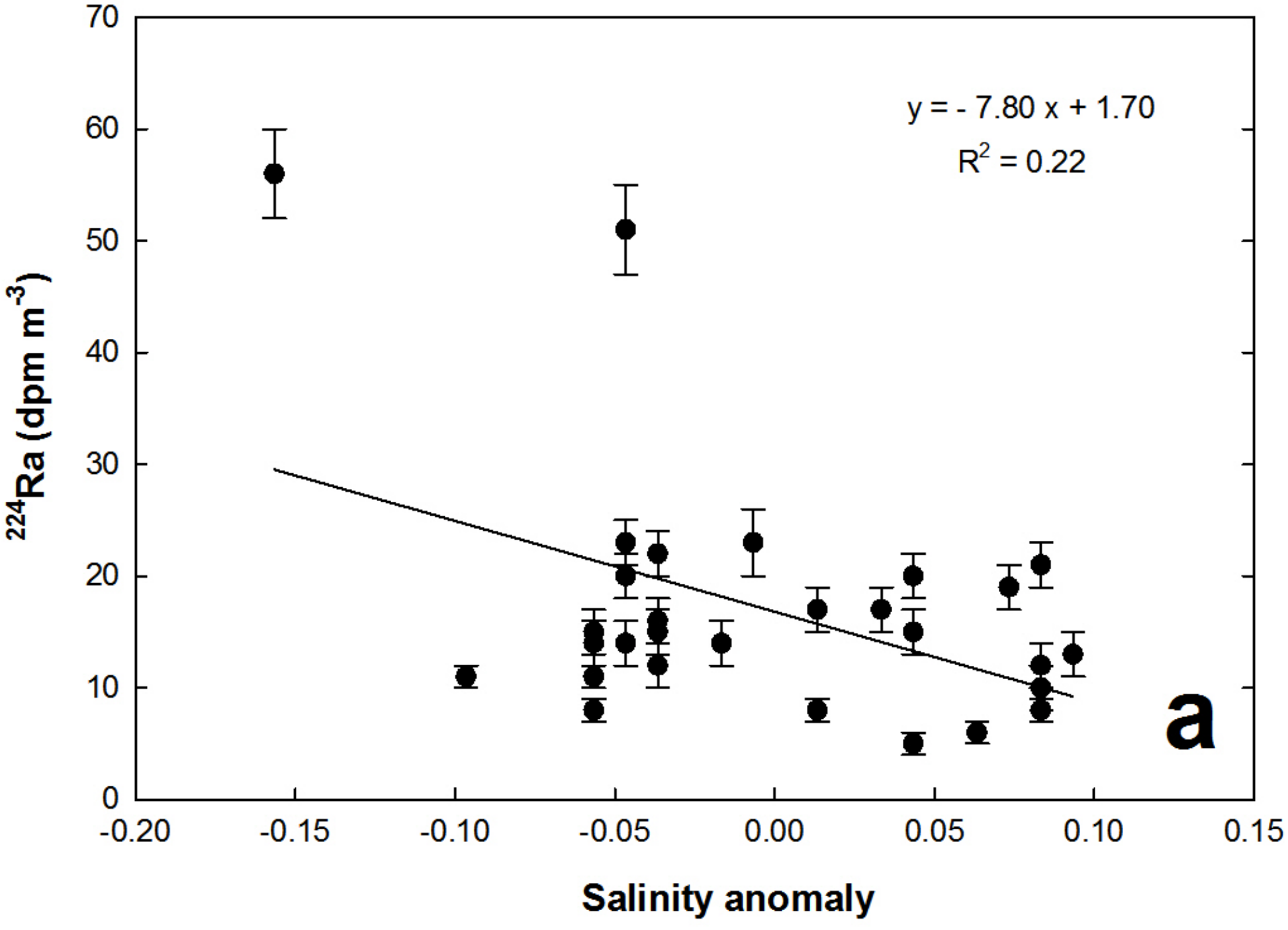
y = - 7.80 x + 1.70
R2 = 0.22
a
224Ra (dpm m-3)
Salinity anomaly
70
60
50
40
30
20
10
0
-0.20
-0.15
-0.10
-0.05
0.00
0.05
0.10
0.15

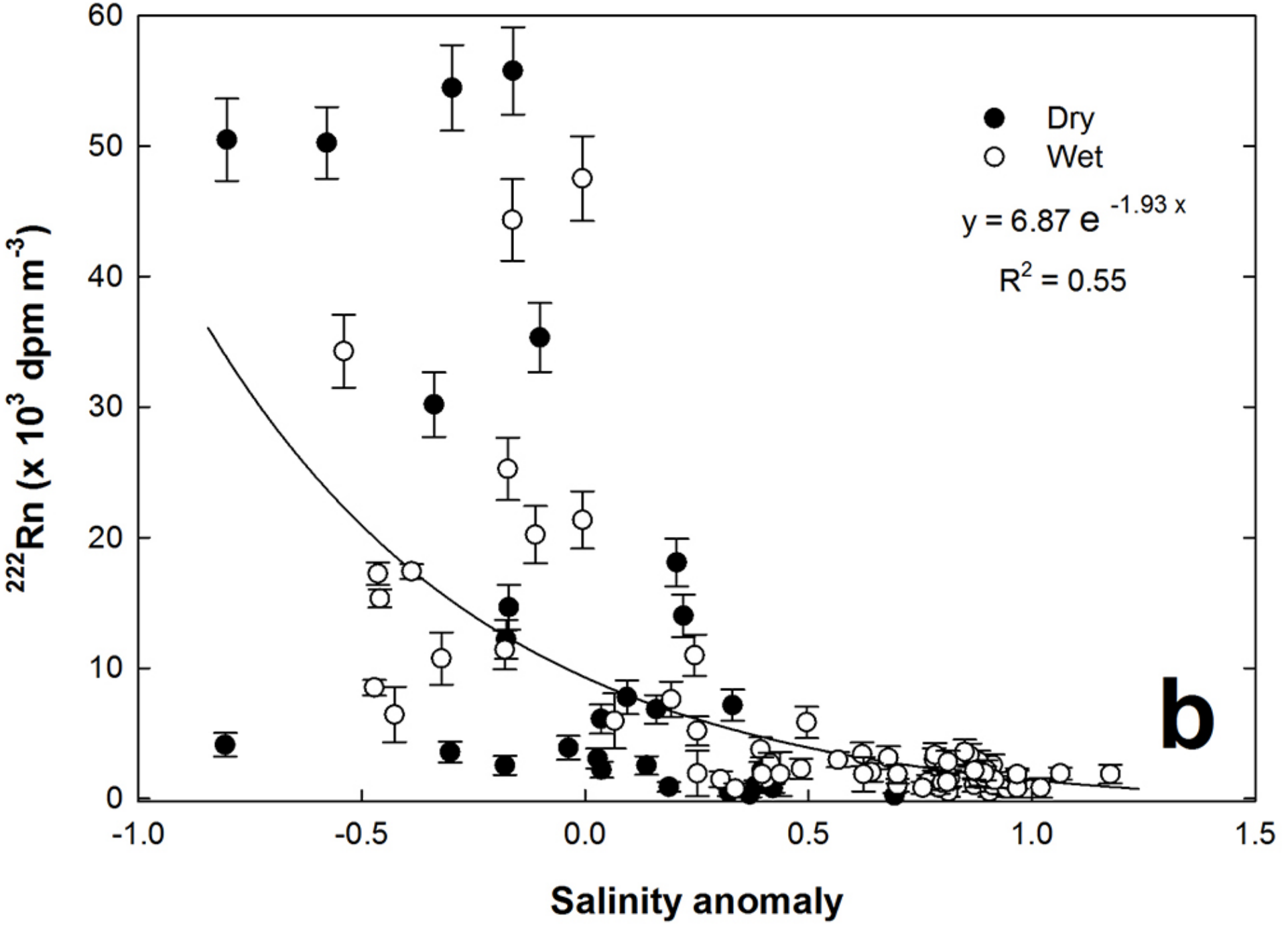
60
50
40
30
20
10
0
-1.0
-0.5
0.0
0.5
1.0
1.5
Dry
Wet
y = 6.87 e -1.93 x
R2 = 0.55
b
222Rn (x 10^3 dpm m^-3)
Salinity anomaly

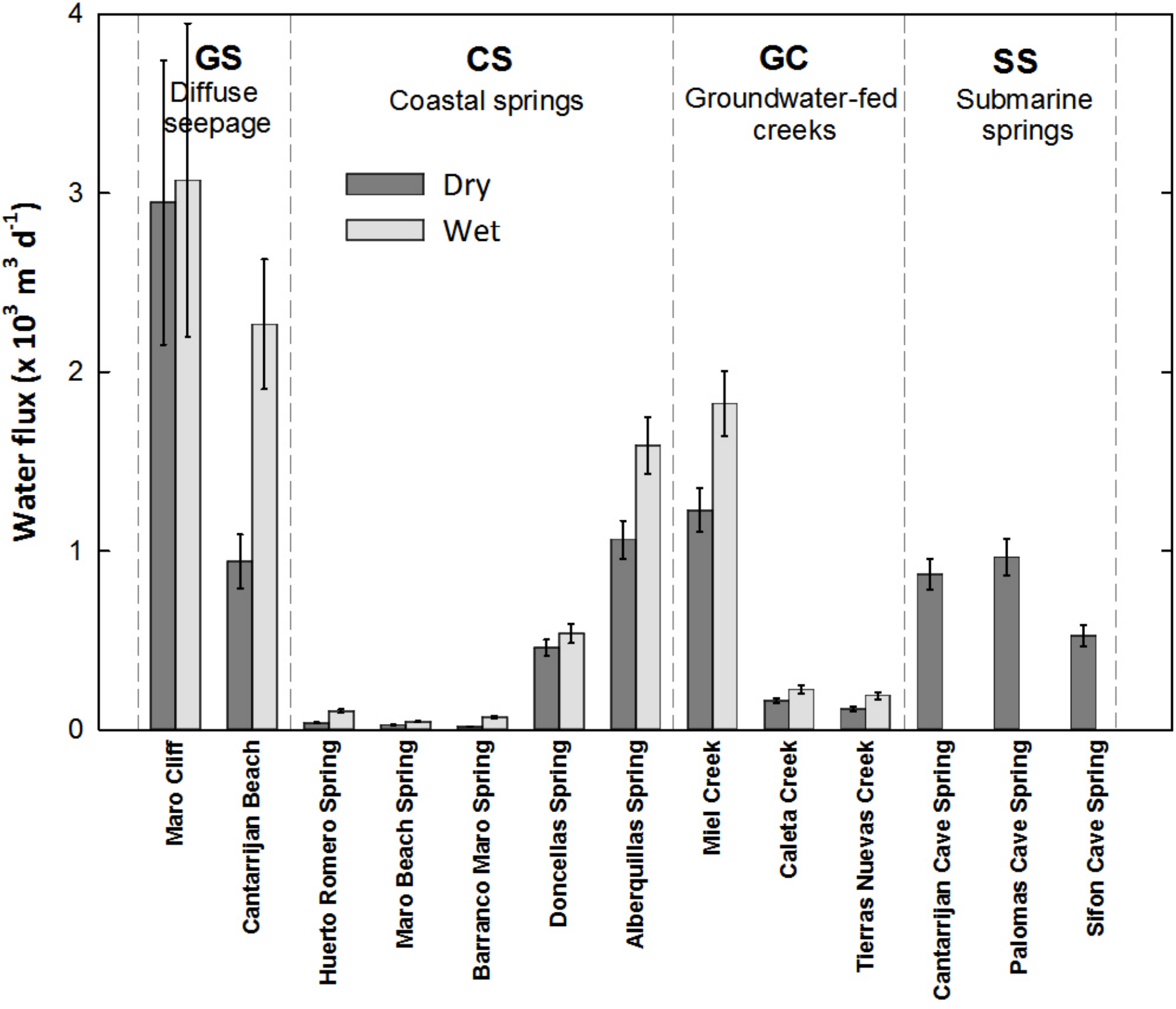
GS
Diffuse seepage
CS
Coastal springs
GC
Groundwater-fed creeks
SS
Submarine springs
Dry
Wet
Water flux (x 10³ m³ d⁻¹)
0
1
2
3
4
Maro Cliff
Cantarrijan Beach
Huerto Romero Spring
Maro Beach Spring
Barranco Maro Spring
Doncellas Spring
Alberquillas Spring
Miel Creek
Caleta Creek
Tierras Nuevas Creek
Cantarrijan Cave Spring
Palomas Cave Spring
Sifon Cave Spring

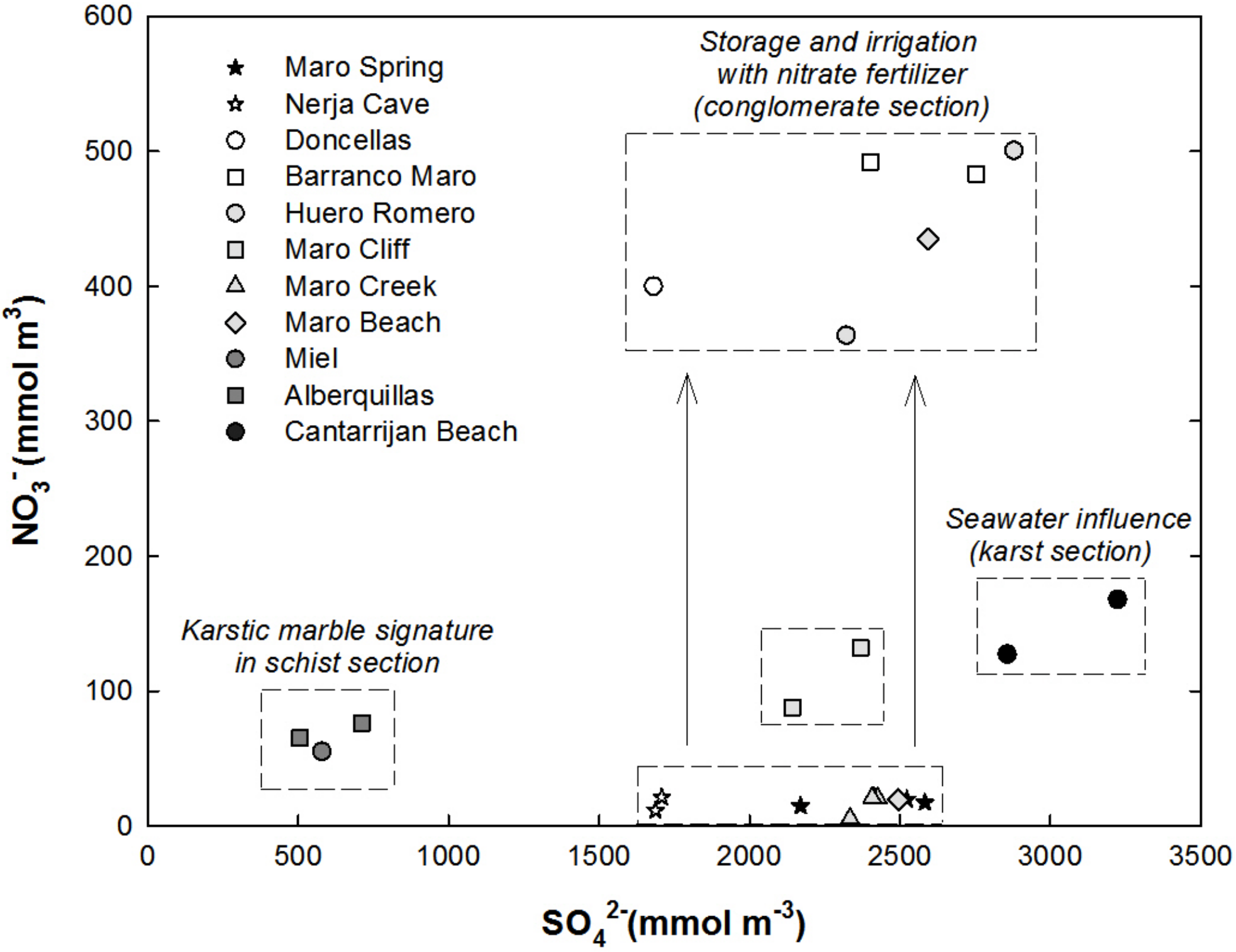
Maro Spring
Nerja Cave
Doncellas
Barranco Maro
Huero Romero
Maro Cliff
Maro Creek
Maro Beach
Miel
Alberquillas
Cantarrijan Beach
Storage and irrigation with nitrate fertilizer (conglomerate section)
Seawater influence (karst section)
Karstic marble signature in schist section
NO_3^- (mmol m^3)
SO_4^{2-}(mmol m^{-3})
0
100
200
300
400
500
600
0
500
1000
1500
2000
2500
3000
3500